Volume 13
Number 40
28 October 2025
Pages 33963–34972

Journal of Materials Chemistry A

Materials for energy and sustainability

rsc.li/materials-a

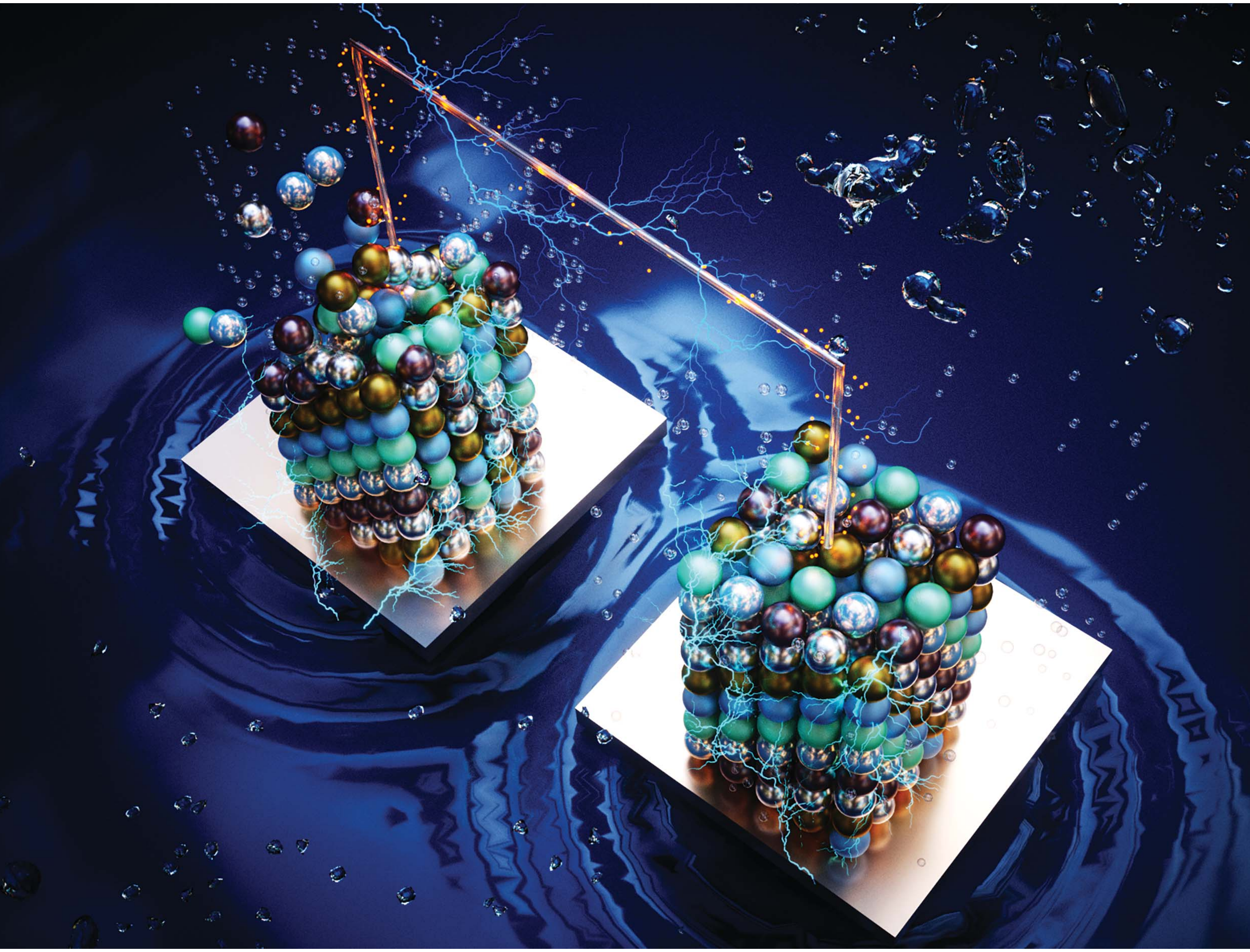

ISSN 2050-7488

ROYAL SOCIETY
OF **CHEMISTRY**

PAPER
Lionel Santinacci, Yaovi Holade, Mikhael Bechelany *et al.*
Atomically bridged palladium between nickel species and carbon microfibers and the subsequent conversion into free-standing and electrocatalytically active multifunctional electrodes

Journal of
Materials Chemistry A

PAPER

Cite this: *J. Mater. Chem. A*, 2025, **13**, 34231

Atomically bridged palladium between nickel species and carbon microfibers and the subsequent conversion into free-standing and electrocatalytically active multifunctional electrodes†

Zahra Hagheh Kavousi,[ab] Clémence Badie,[c] Vyshnav Kannampalli,[c] Massomeh Ghorbanloo,[b] Qing Wang,[d] Hazar Guesmi,[d] Lionel Santinacci,*[c] Yaovi Holade*[aef] and Mikhael Bechelany*[ag]

Received 24th March 2025
Accepted 10th July 2025

DOI: 10.1039/d5ta02374b

rsc.li/materials-a

Biomass-driven water electrolysis at low cell voltage represents an energy-efficient and environmentally friendly technology capable of simultaneously producing hydrogen and generating value-added chemicals. Designing highly active, multifunctional and cost-effective electrocatalysts for the oxidation of alcohols plays a significant role in the development of direct alcohol fuel cells and electrolyzers. Herein, we introduce free-standing multifunctional electrodes created by combining the atomic layer deposition of palladium (Pd) and nickel oxide (NiO) nanostructures directly onto gas diffusion electrodes (GDEs) and thermal treatment to form nanostructured electrocatalysts. We highlight the advantages of palladium–nickel based bimetallic nanostructured electrodes for the hydrogen evolution reaction (HER), ethanol oxidation reaction (EtOR), and glycerol oxidation reaction (GOR) in both half-cell and hydroxide anion exchange membrane (AEM) electrolyzer configurations. Although the metal loading is very low (20 μg_{Pd} cm^{-2} and 47 μg_{Pd+Ni} cm^{-2}), these electrodes demonstrate high current density at low potentials for the GOR and EtOR, as well as reduced overpotential during the HER. Integrating bimetallic GDE-Pd-Ni as anode and cathode electrodes into a biomass-fueled electrolyzer yields an efficient system. Specifically, GDE-Pd-Ni achieved 10 mA cm^{-2} at 0.69 V and 100 mA cm^{-2} at 1.10 V for an ethanol-fed electrolyzer at 50 °C, and 10 mA cm^{-2} at 0.67 V and 100 mA cm^{-2} at 1.21 V for a glycerol-fed electrolyzer at 70 °C. The present work could inspire the development of other energy materials as both the anode and the cathode in electrolyzers for electrosynthesis of fuels and high-value chemicals, promising a radical improvement in the current design of energy-efficient devices with a significantly reduced environmental footprint.

1. Introduction

Hydrogen (H_2), with its high energy density (142 MJ kg^{-1}), is a promising sustainable energy carrier for future energy systems.[1,2] Achieving the full environmental potential of a hydrogen-based society necessitates its production from renewable resources, such as water or biomass.[3] Water electrolysis powered by renewable electricity emerges as a key method for green hydrogen production, with leading technologies including liquid alkaline water electrolyzers (AWEs), proton exchange membrane water electrolyzers (PEMWEs), and hydroxide anion exchange membrane (AEM) water electrolyzers (AEMWEs).[4] However, the high energy requirements of conventional water electrolyzers, operating in both alkaline and acidic media, are largely due to the four-electron transfer oxygen evolution reaction (OER). This reaction, which consumes a substantial portion of the energy input (with a minimum

---

[a] *Institut Européen des Membranes, IEM, UMR 5635, Univ Montpellier, ENSCM, CNRS, 34090 Montpellier, France. E-mail: yaovi.holade@enscm.fr; mikhael.bechelany@umontpellier.fr*

[b] *Department of Chemistry, Faculty of Sciences, University of Zanjan, Zanjan, Iran*

[c] *Aix Marseille Univ, CNRS, CINaM, Marseille, France. E-mail: lionel.santinacci@univ-amu.fr*

[d] *Institut Charles Gerhardt Montpellier (ICGM) – UMR 5253, University of Montpellier, CNRS, 34090 Montpellier, France*

[e] *French Research Network on Hydrogen (FRH2), Research Federation No. 2044 CNRS, 44322 Nantes Cedex 3, BP 32229, France; Web:* **https://frh2.cnrs.fr/**

[f] *Institut Universitaire de France (IUF), 75005 Paris, France*

[g] *Functional Materials Group, Gulf University for Science and Technology (GUST), Mubarak Al-Abdullah 32093, Kuwait*

† Electronic supplementary information (ESI) available. See DOI: **https://doi.org/10.1039/d5ta02374b**

requirement of $\Delta G = 237.1$ kJ mol^{-1}), presents a notable challenge for the kinetics and the materials to be used at the anode to withstand corrosion under electrochemical potential.[1,5–7] Innovations in electrolysis technology aim to mitigate the inefficiencies associated with the OER. One promising strategy involves utilizing small molecule alcohols derived from biomass (C1, C2, and C3 alcohols), which are more energetically favorable to be oxidized than water due to the presence of reactive hydroxyl groups. This approach enables a less energy-intensive anodic reaction, while leveraging the renewable, non-toxic, and high-energy properties of biomass.[8,9]

The electrocatalytic oxidation of biomass-derived compounds, particularly ethanol and glycerol, has garnered considerable attention due to its potential to enable carbon-neutral processes across various applications, including electricity generation *via* fuel cells, CO_2 conversion, and hydrogen production through low-energy-input electrolyzers.[10–13] Ethanol, produced through the fermentation of biomaterials, and glycerol, a low-value byproduct constituting approximately 10 wt% of biodiesel production, are increasingly abundant due to the rising demand for biodiesel.[14,15] Leveraging the oversupply of ethanol and glycerol offers a strategic opportunity to produce valuable oxidized products.[13,16] Consequently, the development of durable, multifunctional electrocatalysts is essential for optimizing the efficiency of these reactions in electrochemical systems. These advanced electrocatalysts can enhance system performance, reduce material and manufacturing costs, simplify device design, and improve durability in energy conversion technologies, addressing critical challenges in this field.[17,18]

Noble metals and their oxides, known for their exceptional catalytic performance, are considered benchmark materials in electrocatalysis. Among these, Pd-based catalysts are extensively studied in alkaline media for their effectiveness in driving the hydrogen evolution reaction (HER) and alcohol oxidation processes.[19–21] The electrochemical properties of Pd closely resemble those of Pt, including susceptibility to poisoning by reaction intermediates during alcohol electrooxidation. In addition, the high cost of Pd limits its commercial scalability, posing a significant challenge to broader adoption in electrochemical applications. Developing efficient, cost-effective electrocatalysts is therefore crucial for advancing electrolyzer technologies.[22] Enhancing atomic utilization through surface property modifications can reduce the required amount of Pd without compromising catalytic activity or stability.[22,23] A key strategy involves incorporating a secondary non-noble metal to modulate Pd's electronic structure, significantly improving both performance and economic viability.[21] This multimetallic approach leverages synergistic effects, enhancing catalytic properties through electronic modulation. By integrating transition metals such as Ni, Sn, Cu, Fe, Zn, and Ag with Pd, the dependence on noble metals can be reduced while significantly improving electrocatalytic performance by geometric, strain and ligand effects.[24–26] In particular, Ni-based electrocatalysts are notable for their electrochemical stability in alkaline environments and cost-effectiveness, making them especially promising for these applications.[27,28] In alkaline solutions, the Ni(III)/Ni(II) redox center exhibits significant catalytic efficiency in oxidizing various small organic compounds.[29–31] Although considerable research has focused on incorporating a second metal to enhance electrocatalyst performance during the last few years, challenges remain in minimizing metal usage and expanding electrode applications. Developing multifunctional electrocatalysts, especially bimetallic nanoparticles, requires precise control over their properties to meet the specific kinetic and thermodynamic demands of reactions within the electrolysis process. Continued research is essential to fine-tune nickel's role and its synergistic effects within bimetallic PdNi systems for optimized electrocatalytic performance.[17,22,27,28,32] Recently, Li *et al.*[17,22,27,28,32] showed that the electrooxidation of alcohols (ethanol, ethylene glycol and glycerol) can be catalytically tuned by incorporating two oxophilic metals, *e.g.* Sn and Ag, to facilitate the desorption of organic intermediates in order to improve the catalytic activity and durability, achieving a mass activity 8 to 14 times higher for PdSnAg/C compared to monometallic Pd/C. More specifically, the electronic interaction between palladium and the other metals (nickel, tin, and silver) leads to a modification of the electronic structure of the multimetallic electrocatalysts, which exhibits a lower charge transfer resistance and a less strong intermediate bond on the catalyst surface after breaking the C–H and O–H bonds.

A significant challenge in nanoparticle surface engineering is their tendency to aggregate, emphasizing the need for innovative stabilization and functionalization strategies. These strategies are crucial for maximizing their large surface area to enhance catalytic activity and selectivity across various applications.[33] Atomic Layer Deposition (ALD), with its self-limiting growth mechanism through sequential binary reactions between gaseous precursors and a substrate, offers a precise method for conformally coating large-surface-area substrates such as carbon plates, metal foams, nanotubes, porous alumina membranes, and gas diffusion electrodes (GDEs) at the atomic level.[33–37] This layer-by-layer deposition method enables the design of customized electrocatalysts, overcoming the limitations of indirect deposition methods like ionomer and binder use, which often result in nanoparticle isolation and catalytic site degradation.[22,38,39]

To date, this is the first study to report palladium nanoparticles bridged between nickel species and carbon fibers in gas diffusion electrodes by ALD and their subsequent conversion into free-standing, electrocatalytically active multifunctional electrodes with ultra-low metal content (20 μg_{Pd} cm^{-2} and 47 μg_{Pd+Ni} cm^{-2}). Building on preliminary findings,[37,38,40,41] we introduce here the ALD method for the precise deposition of Pd nanoparticles and a NiO film (NiOX, $X = 250$ and 1000 cycles) onto a GDE followed by thermal treatment (TT) to produce free-standing and electrocatalytically active electrodes ready for use in electrolyzers without further steps. This method produces Pd/NiOX nanostructures (GDE-Pd/NiOX-TT, $X = 250$ and 1000 cycles), which exhibit significant improvements in catalytic performance. Integrating NiO with the Pd nanoparticle matrix lowers the onset potential and enhances reaction kinetics at reduced overpotentials, with further improvements observed post-treatment. These developments establish nanostructures as multifunctional, free-standing electrocatalysts for the glycerol and ethanol oxidation reactions (GOR and EtOR, respectively), as well as the HER under alkaline conditions. Precise tuning of the NiO layer thickness and bimetallic composition reveals how reaction kinetics are influenced, offering deeper insights into electrocatalytic performance.[31] Moreover, we unveil a hybrid electrolyzer design where GDE-Pd/NiO1000-TT serves dual roles as both the anode and the cathode, tailored specifically for glycerol-fed and ethanol-fed electrolyzers. This configuration enables simultaneous electro-synthesis of high-value fuels and chemicals, generating hydrogen at the cathode and organic compounds at the anode. The integrated GDE-Pd/NiO1000-TT electrode significantly enhances the flow electrolyzer's efficacy, particularly by increasing electrocatalytic activity at the anode for glycerol and ethanol conversion, while also improving hydrogen production at the cathode. This investigation presents a robust multifunctional catalyst, offering a novel approach to energy-efficient hydrogen generation.

2. Experimental section

2.1. Materials and chemicals

AvCarb MGL190 carbon paper electrodes (190 μm thickness) from Fuel Cell Earth LLC (USA) were used for GDE-based experiments. Chemical reagents, including palladium hexafluoroacetylacetonate (Pd(hfac)$_2$, 95%) and bis(ethylcyclopentadienyl)nickel (Ni(EtCp)$_2$, 98%), were purchased from Sigma-Aldrich and Strem Chemicals, respectively. Isopropanol (C_3H_8O, 99.5%) and glycerol ($C_3H_8O_3$, >99.5%) were sourced from Alfa Aesar. Absolute ethanol (C_2H_5OH, >99.9%) was purchased from VWR International (Fontenay sous Bois, France). Potassium hydroxide (KOH, 99.98% (metals basis)) was procured from Acros Organics. A hydroxide anion exchange membrane (AEM), Sustainion® X37-50 Grade RT (50 μm dry thickness), was procured from Fuel Cell Store (USA). The membrane underwent activation in 1 M KOH for 24 hours at 22 ± 3 °C and was subsequently rinsed thrice with Milli-Q water. For comparisons with a commercial catalyst, benchmark 20 wt% Pd on Vulcan XC-72, referred to as "Pd/C-Vulcan" (20 wt%, 3–4 nm, catalyst BET surface area of ~200 m^2 g^{-1}) was purchased from Premetek Co., USA. N_2 (grade 4.5), Ar (grade 5.0), and 5% H_2 in Ar gases were sourced from Air Liquide, France. Ultrapure water (18.2 MΩ cm resistivity at 20 °C) from a Milli-Q Millipore system and deionized water (>12 MΩ cm resistivity) were used consistently. All reagents and chemicals, of analytical grade, were used as received without further purification. A standardized cleaning method[42] was applied to all glassware used in the electrochemical experiments.

2.2. Nanocatalyst synthesis by ALD

Pd nanoparticles were grown on GDE (3 cm high and 3 cm width) substrates in a horizontal, low-pressure hot-wall reactor *via* an ALD chemical reaction with sequential precursor exposure. The Pd deposition process was based on Pd(hfac)$_2$ and formaldehyde as co-reactants. The canister containing formaldehyde was kept at room temperature. The canister containing Pd(hfac)$_2$ was maintained at 70 °C for injection of a sufficient vapor pressure of the precursor molecules into the reactor. The lines were heated at 100 °C to avoid any condensation. The deposition chamber was set at 220 °C, a temperature carefully selected to remain within the ALD window reported for the Pd(hfac)$_2$/formaldehyde chemistry, ensuring self-limiting surface reactions and avoiding undesired CVD-type growth.[43,44] The typical Pd-ALD cycle consists of a 5 s pulse of Pd(hfac)$_2$, 15 s exposure, and 10 s purge, followed by a 1 s pulse of formaldehyde, 15 s exposure and 60 s purge with Ar. The synthesized electrodes are labeled as GDE-Pd. The nickel oxide layers have been grown by ALD in a hot-wall Fiji 200 reactor (Ultratech/Cambridge Nanotech) employing Ni(EtCp)$_2$ and O_3 as precursors. The reactor temperature was set to 250 °C, consistent with the ALD window reported by Lu *et al.*[45] and the Ni(EtCp)$_2$ canister was maintained at 90 °C. Each ALD cycle consisted of sequential pulses, exposure, and purge periods for Ni(EtCp)$_2$ and O_3, with durations of 2 : 10 : 10 s and 0.2 : 10 : 10 s, respectively. An argon flow was introduced into the Ni(EtCp)$_2$ canister for 1 s prior to the precursor pulse to enhance the transport of reactive species towards the reactor. The ALD process was performed under conditions optimized to ensure surface saturation and uniform growth on the porous GDE substrate. NiO coatings were deposited using either 250 or 1000 cycles to explore the effect of oxide loading on electrocatalytic performance. These cycle numbers correspond to thicknesses of 6 and 24 nm, respectively, as measured on planar Si wafers placed alongside the GDE (GPC ~0.22 Å per cycle, see Fig. S1†).[45] These two thicknesses were targeted to get an ultra-thin layer (6 nm) and a thicker film (24 nm) with bulkier properties. After deposition, the samples underwent thermal treatment in a 5% hydrogen–argon gas atmosphere at 500 °C for 2 h, with the temperature ramped at a rate of 10 °C per minute.

2.3. Physico–chemical characterization

To determine the thickness of the NiO films following ALD, *in situ* spectroscopic ellipsometry (SE) measurements were performed using an M-2000 V (J. A. Woollam Co). Curve fitting was performed using CompleteEASE 5.10 software. The morphology of the catalysts was evaluated using scanning electron microscopy (SEM) on a Hitachi S4800 microscope. Elemental distribution was analyzed through energy-dispersive X-ray (EDX) spectroscopy using a ZEISS EVOHD 15 microscope. The surface structure of the catalysts was characterized by transmission electron microscopy using a JEOL 2100F. Samples for TEM analysis were dispersed in ethanol by ultrasonication and then deposited onto a holey carbon film supported by a copper grid. Bulk elemental quantification was conducted using inductively coupled plasma optical emission spectrometry (ICP-OES) on an Agilent 5110 VDV spectrometer. XPS analysis was performed on a Kratos Axis Ultra (Kratos Analytical, UK). The spectrometer is equipped with a monochromatic Al Kα source (1486.6 eV). All spectra were recorded at a 90° take-off angle, with an analyzed area of about 0.7 × 0.3 mm. Survey spectra were acquired with a 1.0 eV step and 160 eV analyzer pass energy. The high-resolution regions were acquired with a 0.1 eV step (0.05 eV for O 1s and C 1s) and 20 eV pass energy. A neutralizer was used to perform the recording to compensate for the charge effects. Curves were fitted using a Gaussian/Lorentzian (70/30) peak shape after Shirley's background subtraction and using CasaXPS software. The carbon C 1s is calibrated at 284.8 eV for C–C and C–H bonds.

2.4. Density functional theory (DFT) calculations

DFT calculations were performed using the Vienna *Ab initio* Simulation Package (VASP).[46] The exchange–correlation interactions were treated within the generalized gradient approximation (GGA) using the Perdew–Burke–Ernzerhof (PBE) functional.[47] Electron–ion interactions were described with the projector augmented-wave (PAW) method.[48,49] A plane-wave basis set with a kinetic energy cutoff of 400 eV was employed. To improve the description of localized Ni 3d electrons, a Hubbard U correction was applied. An effective U value of $U_{\text{eff}} = U - J = 5.3$ eV (with $U = 6.3$ eV and $J = 1.0$ eV) was adopted, following values reported in the literature.[50] The pristine Pd(111) surface was modeled by cleaving a $(\sqrt{13} \times \sqrt{13})$ R13.9° supercell slab from bulk face-centered cubic (fcc) palladium, composed of five atomic layers (13 atoms per layer), with a vacuum region of 15 Å to avoid interaction between periodic images. This specific supercell was chosen to minimize the lattice mismatch with the NiO(111) overlayer, as the rotated $\sqrt{13} \times \sqrt{13}$ configuration provides a nearly commensurate interface with low interfacial strain (~1–2%), enabling accurate structural and electronic modeling of the oxide–metal interface. Similarly, the Ni–O layer was generated by cleaving a NiO(111) surface from bulk NiO (fcc structure). The calculated equilibrium lattice constants were 3.88 Å for Pd and 4.12 Å for NiO. During structural relaxations, the two bottom Pd layers were kept fixed at their bulk positions, while the upper layers including Ni–O atoms were fully relaxed until residual atomic forces were below 0.02 eV Å^{-1} and the energy convergence criterion was set to 10^{-6} eV. Brillouin zone sampling was performed using a 5 × 5 × 1 Monkhorst–Pack k-point mesh. Dispersion interactions were considered using the DFT-D3 method of Grimme.[51] Electronic properties were analyzed *via* the projected density of states (PDOS), and the d-band center (ε_d) was calculated according to:

$$\varepsilon_{\text{d}} = \int E.\text{DOS}_{\text{d}}(E)\text{d}E / \int \text{DOS}_{\text{d}}(E)\text{d}E$$

where $\text{DOS}_{\text{d}}(E)$ represents the density of d-states at energy E.

Bader charge analysis was also performed to quantify the electron transfer between the Ni–O layer and the Pd atoms.

2.5. Electrochemical characterization in a half-cell

All electrochemical characterization studies were performed using an SP-150 potentiostat from Biologic Science Instruments. The catalytic capabilities of GDE-Pd/NiOX and GDE-Pd/NiO*X*-TT (X = 250 and 1000 cycles) electrodes for the GOR, EtOR, and HER were evaluated in a standard three-electrode cell with a single compartment. This setup included the GDE-Pd/NiOX electrode (0.5 cm × 1 cm) as the working electrode, a glassy carbon electrode (5 cm^2) as the counter electrode, and a mercury/mercury oxide (Hg/HgO, MOE) as the reference electrode. To test the commercial 20 wt% Pd/C catalyst, under identical metal loading conditions onto a GDE as the as-synthesized GDE-Pd (see Table S2† to reach 32 μg$_{\text{Pd}}$ cm^{-2}), a catalytic ink was prepared by ultrasonically mixing 130 μL MQ water, 50 μL iPrOH, 20 μL Nafion® suspension and 1 mg catalyst before drop-casting a suitable volume onto each face of a bare L-shaped GDE of similar size (0.5 cm × 1 cm) to reach 32 μg$_{\text{Pd}}$ cm^{-2}. Electrochemical measurements were taken in 1 M KOH solution, saturated with Ar and containing 1 M glycerol for the GOR or 1 M ethanol for the EtOR, at a temperature of 25 °C. To activate and stabilize the electrodes, cyclic voltammetry (CV) was executed over 19 cycles at a scan rate of 100 mV s^{-1}. HER assessments were conducted *via* linear sweep voltammetry (LSV) at a scan rate of 5 mV s^{-1}. Furthermore, potentiostatic electrochemical impedance spectroscopy (EIS) analysis spanned frequencies from 100 kHz to 100 mHz at various potentials. The study standardizes all potentials to the reversible hydrogen electrode (RHE) scale for uniformity and ease of comparison, using the conversion formula $E(V\ vs.\ \text{RHE}) = E(V\ vs.\ \text{MOE}) + 0.92$. The reported potentials are not corrected for ohmic drop (the ohmic resistance was approximately 2.6 Ω cm^2).

Long-term HER stability was determined in a two-compartment H-type cell (1 M KOH electrolyte, 2 cm^2 GDE-Pd/NiO1000-TT electrode as the working electrode area, 10 cm^2 glassy carbon as the counter electrode, Sustainion® X37-50 Grade RT hydroxide AEM as the separator, temperature of 25 °C, with periodic electrolyte renewal of both the anolyte (40 mL) and the catholyte (40 mL)). We implemented the galvanostatic method at an applied current of $|I_{\text{appl}}| = 100$ mA (corresponding to a current density of $|j_{\text{appl}}| = 50$ mA cm^{-2}). We implemented ICP-OES analysis to track possible Ni and/or Pd dissolution.

2.6. Long-term electrolysis in a hydroxide AEM based H-type cell and high-performance liquid chromatography (HPLC)

Long-term bulk electrolysis for the GOR and product distribution analysis was conducted in a two-compartment H-type cell. The setup utilized a multi-channel VSP-3e potentiostat (Biologic Science Instruments) at an applied current of 10 mA cm^{-2} for a duration of 12 hours. The anodic compartment, containing a 1 cm^2 GDE-Pd/NiO1000-TT electrode, was filled with 1 M KOH and 1 M glycerol (40 mL), while the cathodic compartment housed a 1 cm^2 GDE-Pd/NiO1000-TT electrode in 1 M KOH (40 mL). The two compartments were separated by a Sustainion® X37-50 Grade RT hydroxide AEM, with anode and cathode potentials monitored during galvanostatic operation by inserting a miniature reference electrode (RHE, MiniHydroFlex®, BioLogic) in each compartment. Glycerol electrooxidation products were identified and quantified using HPLC on a Dionex ICS-1000 system. Organic acids were separated by pK_{a} using a BP-OA Benson 2000-0 column and detected at 210 nm with a UV-vis detector. The injection volume was set to 25 μL, with an eluent of 25 mM H_2SO_4 flowing at 0.4 mL min^{-1}. Separation was achieved based on retention times, with product quantification *via* peak area analysis. Calibration curves for expected reaction products, including oxalic acid, tartronic acid, glyceric acid, glycolic acid, and formic acid, were established with concentrations from 0.05 mM to 2 mM, showing linear regression ($R^2 > 0.999$). To protect the column's stationary phase, samples were diluted with ultrapure water to reduce alkalinity.

2.7. Zero-gap hydroxide AEM based electrolyzer

Zero-gap hydroxide AEM-based electrolyzers, controlled by an SP-150 potentiostat (Biologic Science Instruments) equipped with a 10 A/20 V booster (VMP3B-10, Biologic Science Instruments), were utilized for the electrolysis of biomass-derived compounds. Integrated heating elements and a thermocouple within the end plates facilitated precise temperature control. The electrolysis cell's total active area spanned 5 cm^2, with pairs of GDE-Pd/NiO1000-TT electrodes acting as multifunctional electrocatalysts, positioned on either side of the AEM. The cell assembly underwent mechanical compression and temperature stabilization at 25, 50 and 70 °C. Operational parameters included a catholyte flow rate of 45 mL min^{-1} using 1 M KOH and an anolyte flow rate of 23 mL min^{-1} with a mixture of 1 M KOH and 1 M glycerol (or 1 M ethanol), propelled by gear pumps. Both recirculation solutions were temperature-regulated in a water bath at the same temperature (*i.e.*, 25, 50 or 70 °C). Electrochemical performance assessment utilized two methodologies: LSV at a scan rate of 0.05 V s^{-1} and potentiostatic evaluation with 0.1 V potential steps for varied durations. Hydrogen output was quantified using the water displacement technique, allowing real-time measurement of hydrogen production when a consistent current (250 mA, equivalent to 50 mA cm^{-2} for comparative analysis across all electrodes) was applied. The observed hydrogen flow rates were calculated and contrasted with theoretical values predicted using Faraday's law. The activation energy (E_a) for the GOR was determined by measuring the temperature dependence (25, 50 and 70 °C) using a thermal bath system. Assuming that charge transfer resistance follows a thermally activated process, its sensitivity to temperature can be analyzed using the Arrhenius equation:

$$\ln R_{\mathrm{ct}} = \frac{E_{\mathrm{a}}}{RT} - \ln R_0 \quad (1)$$

where R_{ct} is the charge transfer resistance at a specific potential, R is the universal gas constant, T is the temperature in Kelvin, and E_a is the apparent activation energy. E_a can be determined from the slope of a linear plot of $\ln R_{\mathrm{ct}}$ *versus* T^{-1}.[52]

3. Results and discussion

3.1. Synthesis and characterization

GDE-Pd/NiO*X* ($X = 250$ and 1000 cycles) electrodes were fabricated by successive ALD of Pd and NiO.[38,40,53] After deposition, the samples were thermally treated under a 5% hydrogen–argon atmosphere at 500 °C, to enhance crystallinity, promote alloying, and remove residual organics from the ALD process while preserving nanoparticle dispersion. Previous studies on Pd/Ni based nanocatalysts have shown that lower temperature treatments (~200 °C) effectively reduce PdO to metallic Pd but are insufficient to promote alloying or substantial surface activation. Increasing the treatment temperature to 500 °C enables enhanced crystallinity and partial Pd–NiO alloy formation.[54] Supporting studies reported that Pd nanoparticles treated at 500 °C exhibited only a slight increase in average size and retained a high particle density, consistent with Ostwald ripening as the dominant sintering mechanism. In contrast, annealing at higher temperatures (*e.g.*, 750 °C) led to substantial coalescence, particle growth, and loss of active surface area.[55] Scanning electron microscopy (SEM) was employed to analyze the morphology of particles and films on the GDE both before and after thermal treatment, as shown in Fig. 1 and S2–3.† Before thermal treatment, Pd nanoparticles were embedded within a NiO layer covering the carbon fibers. As illustrated in Fig. S2,† increasing the NiO deposition cycles from 250 to 1000 resulted in enhanced film coverage on carbon fibers, consistent with ALD's self-limiting nature that allows precise control over film thickness. Comparing Fig. 1a and c, the latter displays a more granular and dense morphology with agglomeration, likely due to increased NiO thickness promoting particle coalescence from higher surface energy and decreased surface area-to-volume ratio. Although the three-dimensional (3D) GDE substrate offers a high surface area—advantageous for electrocatalysis due to increased active sites—it is susceptible to nanoparticle agglomeration and sintering, which reduce the surface area and power capabilities.[56] Additionally, the carbon substrate may influence growth behavior due to its lack of hydroxyl (–OH) functional groups, which are typically required for initiating ALD reactions through surface adsorption. This could lead to preferential growth on previously deposited NiO layers, forming particles rather than a continuous film. After treatment, partial reduction and restructuring of the NiO layer lead to the coexistence of NiO and metallic Ni on the surface, forming a mixed oxide–metal interface, as evidenced by EDS mapping in Fig. S3,† which highlights a reduction in oxygen content. These morphological changes are attributed to dewetting phenomena and restructuring of the NiO/Ni layer. High-temperature dewetting causes the continuous NiO film to break into isolated islands or particles, resulting in a more granular morphology and the redistribution of Pd nanoparticles. The transformation mechanism, described by Richardson *et al.*,[57] involves hydrogen dissociating on Ni atoms adjacent to oxygen vacancies, facilitating Ni–O bond rupture and water desorption, which promotes nucleation and growth of Ni. The reaction progresses auto-catalytically as Ni clusters grow into larger crystallites. Surface water vapor, influenced by sample geometry, modulates the reaction rate, highlighting the interplay between molecular processes and morphological outcomes.[58] Elemental mapping complemented these findings by illustrating the spatial distribution of Ni, Pd, O, and C. The presence of carbon, as expected, was attributed to the GDE structure, mirroring the elemental distribution patterns observed in SEM-based imaging (Fig. S3 and Table S1†). The absence of detectable Ni in EDX mapping within the GDE-Pd/NiO250 sample before thermal treatment likely results from the extremely thin and uniformly dispersed NiO layer produced by ALD, especially at lower cycle counts since Ni is visible on GDE-Pd/NiO1000. This thin, highly dispersed layer can lead to Ni concentrations

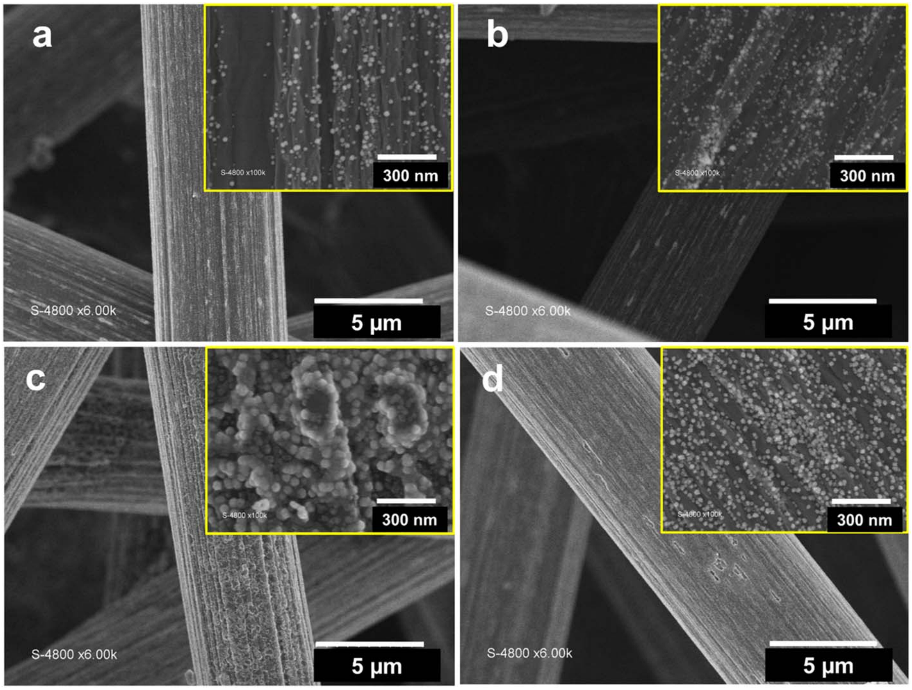

Fig. 1 SEM images of GDE-Pd/NiO$_x$ (before and after thermal treatment) deposited on a GDE (3×3 cm^2) at different thicknesses: (a) GDE-Pd/NiO250, (b) GDE-Pd/NiO250-TT, (c) GDE-Pd/NiO1000, and (d) GDE-Pd/NiO1000-TT.

below the detection threshold of EDX (Tables S1–2†). Following thermal treatment, the reduction and aggregation of NiO into larger metallic Ni particles increase both the local Ni concentration and particle size, making them detectable in post-treatment EDX mapping (Fig. S3†).

Further detailed investigations into the structural and morphological properties of the bimetallic GDE-Pd/NiO samples were conducted using transmission electron microscopy (TEM), employing a scratching technique. As outlined in Fig. 2, TEM analysis for GDE-Pd/NiO250-TT revealed that Pd nanoparticles were embedded within a NiO film, with thickness varying across the sample, showcasing a wide range of particle sizes from 5 to over 10 nm (Fig. 2a1–a2). The presence of Pd nanoparticles on the surface after thermal treatment indicates that the high-temperature reducing atmosphere facilitates structural rearrangements, leading to the formation and redistribution of nanoparticles. The thermal energy provided during treatment allows for atom mobility, promoting the nucleation and growth of Pd nanoparticles within the NiO matrix. The NiO layer, predominantly found on the surface, exhibits a differential deposition pattern that likely influences the electrode's overall electrochemical performance. The non-uniform deposition of the NiO layer can affect the accessibility of Pd nanoparticles to reactants and the overall conductivity of the electrode.

In the reduced layer of the GDE-Pd/NiO1000-TT variant, there was not only a reduction in aggregation but also an increase in the uniformity of nanoparticle sizes, with smaller particles being more prevalent. This observation could be explained by the thermal treatment under a hydrogen atmosphere, which may partially reduce NiO to metallic Ni. This partial reduction could stabilize the nanoparticles and mitigate aggregation through strong metal–support interactions, potentially inhibiting particle coalescence. These detailed TEM observations provide crucial insights into the structural evolution and its impact on the functionality of the electrodes, particularly after thermal treatment. Understanding the morphological changes and the interactions between Pd and Ni (or NiO) at the nanoscale is essential for optimizing the electrocatalytic properties of the electrodes. The size, distribution, and composition of the nanoparticles directly influence the catalytic activity and stability, as they affect adsorption energies, electron transfer rates, and the availability of active sites.

X-ray photoelectron spectroscopy (XPS) was conducted to analyze the electronic structure and chemical states of Pd and Ni in both configurations (monometallic and bimetallic after thermal treatment). Fig. S4† shows the survey spectra, highlighting the presence of Pd, Ni, O, and C elements in GDE-Pd, GDE-NiO1000-TT, and GDE-Pd/NiO1000-TT samples. The high-resolution XPS spectra of the GDE-NiO1000-TT sample revealed a primary peak corresponding to Ni $2p_{3/2}$, along with characteristic satellite peaks around 855 eV adjoining the main peaks, owing to the multi-electron excitations. These main peaks were further deconvoluted into sub-peaks indicative of various oxidation states, including metallic nickel (Ni^0) at 852.73 eV and nickel oxide and hydroxide species ($Ni^{2+}O$ and $Ni^{2+}(OH)_2$) at 855.69 eV.[59,60] Similarly, the GDE-Pd sample exhibited two principal peaks corresponding to Pd $3d_{5/2}$ and Pd $3d_{3/2}$, which were further resolved into spin–orbit peaks representing both metallic palladium (Pd^0) at binding energies of 335.12 and 340.21 eV and palladium oxide species (Pd^{2+} and Pd^{4+}) at 336.18 and 341.49 eV, respectively (Fig. 3).[40,61] The

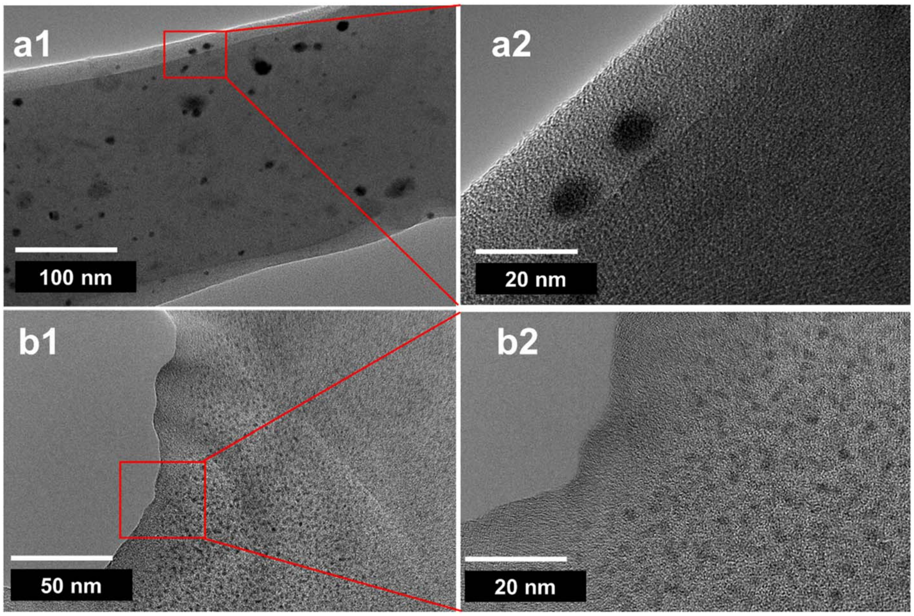

Fig. 2 TEM images of (a1–a2) GDE-Pd/NiO250-TT and (b1–b2) GDE-Pd/NiO1000-TT.

coexistence of metallic Pd and oxidized Pd species indicates that Pd is partially oxidized, possibly due to exposure to air or residual oxygen during the deposition.

XPS analysis of bimetallic GDE-Pd/NiO1000-TT electrodes reveals significant differences compared to monometallic samples. The electrodes display combined features of both Pd and Ni peaks with minor alterations in peak positions and intensities showing the partial reduction. Interactions between Pd and Ni atoms lead to a redistribution of electron density due to electronic hybridization and possible alloy formation, modifying the electronic structure. This manifests as shifts in binding energies and changes in peak shapes in the XPS spectra, also evidenced by shifts in peak positions in XRD results (Fig. S5†). In the bimetallic samples, the characteristic Pd $3d_{5/2}$ and $3d_{3/2}$ peaks remain, while sub-peaks corresponding to oxidized Pd species are significantly diminished or absent (PdO_2 species). This suggests a reduction of Pd oxides and a homogenization of Pd electronic states, likely due to partial alloy formation with Ni and the reductive effect of thermal treatment under hydrogen. For Ni, the $2p_{3/2}$ peaks remain, but the sub-peaks indicative of the metallic Ni show reduced intensity relative to the monometallic Ni sample. This suggests partial oxidation of Ni or a decreased proportion of metallic Ni in the bimetallic system. The presence of Pd contributes to this effect through electronic interactions that alter the local electronic environment and oxidation states of Ni atoms. Possible electron transfers from Ni to Pd in the alloy could lead to slight Ni oxidation and Pd reduction, modifying their chemical states. The thermal treatment restructures the NiO layer and redistributes Pd nanoparticles, affecting the

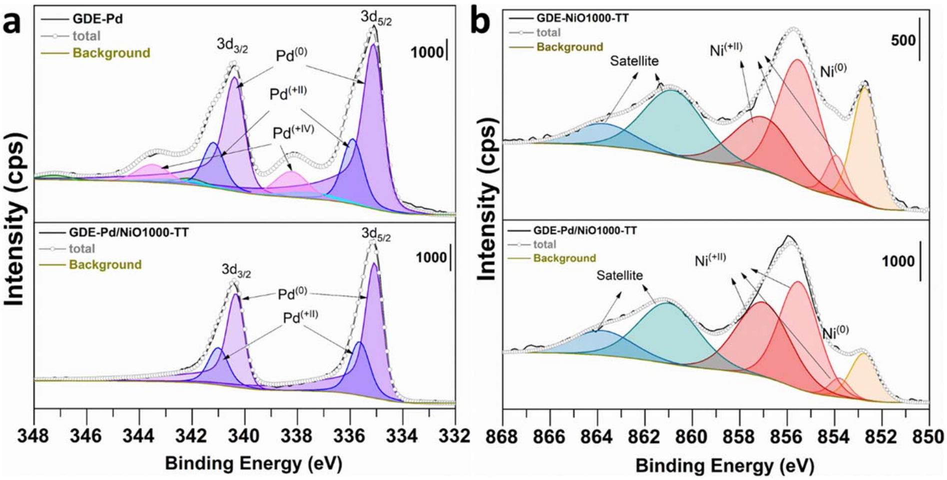

Fig. 3 High-resolution XPS spectra of the GDE-Pd/NiOX material: (a) Pd 3d XPS spectra of GDE-Pd (top) and GDE-Pd/NiO1000-TT (bottom), and (b) Ni 2p XPS spectra of GDE-NiO1000-TT (top) and GDE-Pd/NiO1000-TT (bottom).

electrode's stability and activity. Morphological transformations lead to a more uniform distribution of smaller nanoparticles across the substrate, as evidenced by SEM and TEM analyses. This uniform dispersion increases the active surface area, enhances mass transport, and reduces particle aggregation during operation, thereby improving catalytic efficiency and stability.

We next sought to support the experimental observations of the palladium electronic environment modification induced by the incorporation of NiO by DFT calculations. Specifically, the Pd(111) surface (representative of the synthesized palladium nanoparticles) was modelled, either with a NiO overlayer or with a Ni–O layer intercalated between two Pd(111) layers. The electronic structure analysis of Fig. 4a revealed that for pristine Pd(111), the d-band center is located at −1.72 eV. Upon deposition of a NiO layer directly on top of the Pd(111) surface, the d-band center shifts significantly to −2.11, thus supporting the modification of the electronic structure of palladium. Such a Pd@NiO core–shell structure models the first scenario where reduction heat treatment (as in electrochemical applications) does not affect atom diffusion or surface reorganization. It should be noted that Pd was first deposited on a GDE, followed by NiO deposition and then reduction heat treatment.

In the second scenario, where heat-driven reduction (as well as electrochemical applications) would result in atom diffusion or surface reorganization, which is likely, the surface structure could be modeled using Pd@NiO@Pd as well as $PdNi_x$@NiO@Pd. So, Fig. 4b shows that when the NiO layer is inserted beneath the uppermost Pd(111) layer, the d-band center of the topmost Pd atoms is found at −1.96 eV, while that of the Pd atoms situated below the Ni–O layer (third layer) further shifts to −2.30 eV. Both d-band center positions are negatively shifted. Furthermore, Fig. 4c and d show the Bader charge density difference illustrating the redistribution of electronic density upon the addition/intercalation of the NiO layer over/in the Pd(111) surface. Significant electron accumulation is observed at the NiO/Pd interface, while depletion appears around the Ni atoms and the Pd atoms just below the Ni. This indicates strong interaction between Pd and the underlying NiO species. Altogether, these DFT results corroborate the XPS findings, demonstrating that NiO incorporation induces significant electronic modulation of Pd, which can directly influence its catalytic behavior.

3.2. Electrochemical characterization and analyses

3.2.1. Electrocatalytic HER performance. The electrochemical characterization of various electrocatalysts was conducted using cyclic voltammetry (CV) at a potential scan rate of 100 mV s^{-1} (Fig. S6†). This procedure was conducted in a 1 M KOH electrolyte at 25 °C. As shown in Fig. S6,† for the GDE-Pd

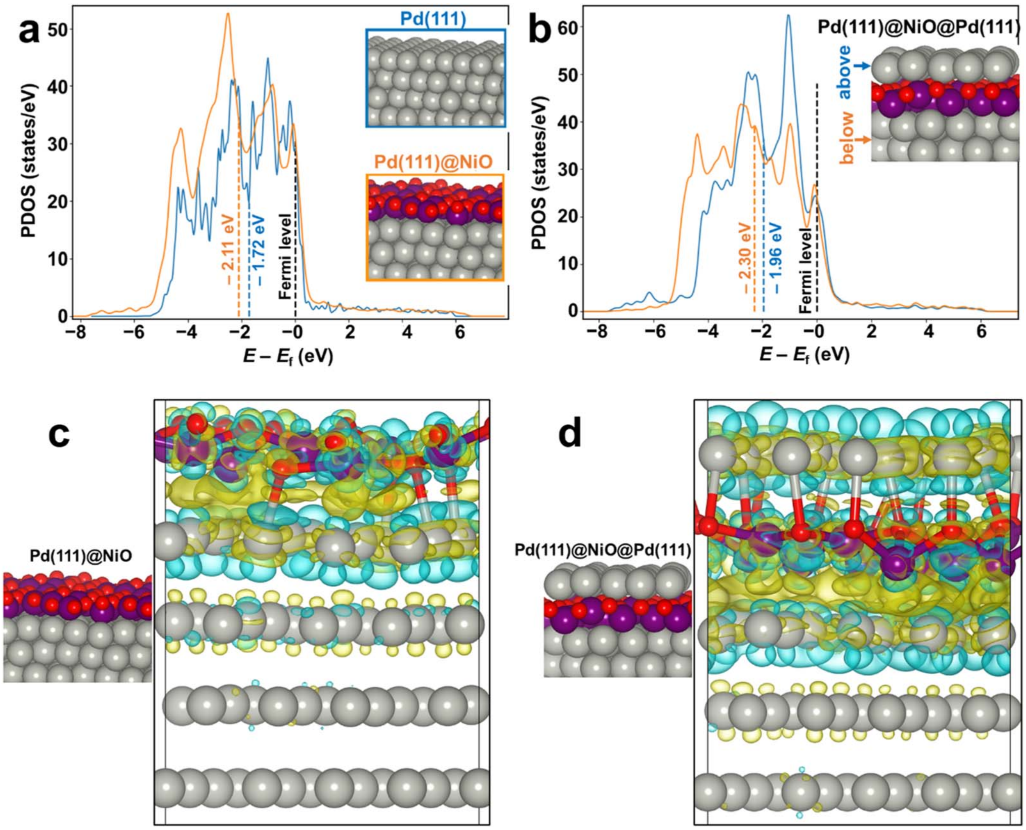

Fig. 4 DFT calculations. Projected density of states of Pd atoms: (a) surface Pd d-bands before and after the deposition of the NiO layer and (b) Pd d-bands above and below the NiO sandwich layer. The colored dashed lines indicate the position of d-band centers. Bader charge density difference isosurfaces (the isosurface value is set to 0.004) illustrating the distribution of electronic density for (c) the NiO layer on top of Pd layers and (d) the NiO layer sandwiched between Pd layers. Red, purple and grey colored balls present O, Ni and Pd atoms, respectively.

sample, the CV profile shows Pd characteristics, with Pd oxidation at around 0.70 V *vs.* RHE and PdO reduction to Pd at about 0.65 V *vs.* RHE.[62] In GDE-NiO*X* deposited samples, redox peaks for the Ni(III)/Ni(II) couple appear between 1.3 and 1.4 V *vs.* RHE.[63] The bimetallic GDE-Pd/NiOX samples combine features of both Pd and Ni,[27,64,65] with enhanced redox peak intensities after thermal treatment. Following the CV activation, the electrocatalytic performance of different GDE-based catalysts towards the HER was evaluated through linear sweep voltammetry (LSV), with overpotential (η) measurements taken at a current density of $|j| = 10$ mA cm^{-2}. A slow sweep rate of 5 mV s^{-1} was employed to ensure quasi-steady-state conditions and to minimize the influence of capacitive current. The LSV curves in Fig. 5a reveal that single metal-based electrodes (*e.g.*, GDE-Pd and GDE-NiO1000 at 0.4 and 0.46 V *vs.* RHE, respectively) exhibit higher overpotentials compared to bimetallic-based electrodes (*e.g.*, GDE-Pd/NiO1000 at 0.27 V *vs.* RHE). This highlights the synergistic effect of introducing NiO into Pd-based electrodes. The addition of NiO modifies the electronic structure of Pd (shift in binding energy evidenced by XPS analysis), facilitating more efficient hydrogen adsorption and desorption processes, as evidenced by the shift in the LSV curve towards lower overpotentials in the presence of NiO. Thermal treatment plays a critical role in transforming the structure and optimizing the performance of GDE-Pd/NiO*X* electrodes. Specifically, treated bimetallic catalysts, GDE-Pd/NiO250-TT and GDE-Pd/NiO1000-TT, exhibited lower overpotentials (0.29 and 0.26 V *vs.* RHE, respectively) to achieve the benchmark current density of $|j| = 10$ mA cm^{-2} compared to their non-treated counterparts (0.31 and 0.27 V *vs.* RHE, respectively). Post-treatment, the nanoparticles become smaller and more evenly distributed across the substrate, forming a nanostructured arrangement that substantially increases the surface area available for catalytic activities. The formation of an Ni/NiO layer and redistribution of the Pd particles during thermal treatment further stabilizes the nanoparticles, preventing agglomeration and enhancing catalytic activity by providing additional active sites and improving catalytic activity and stability (Fig. 5b). Electrochemical impedance spectroscopy (EIS) analyses (Fig. 5c) further support these findings, where lower charge-transfer resistances correspond to the thermally treated bimetallic sample, signifying an improved electron transfer process, which is essential for efficient catalysis and coincides well with the overpotential values for the HER (gathered in Table S3†). EIS fitted data are reported in Table S3,† in which the equivalent electrochemical circuit was $R_\Omega + Q_{\mathrm{CPE}}//R_{\mathrm{ct}}$, where R_Ω is naturally the total ohmic resistance (cell resistance), R_{ct} is the charge transfer resistance, and Q_{CPE} is the capacitance of the constant phase element. To describe the reaction mechanism, the R_{ct}-based Tafel plots from EIS were also obtained. The Tafel slope of 119–168 mV dec^{-1} (Fig. S7†) indicates that they undergo the Volmer–Heyrovsky HER mechanism and the initial adsorption of hydrogen atoms from water splitting on the catalyst surface would be the rate-determining step ($H_2O + e^- \rightarrow H_{(ads)} + OH^-$, Volmer reaction).

3.2.2 Electrocatalytic EtOR performance. The electro-oxidation of ethanol holds significant potential in biomass-fed electrolyzers and direct alcohol fuel cells due to its dual role in energy conversion and chemical synthesis.[66,67] This process not only generates electrical energy but also produces valuable chemicals. To enhance efficiency and simplify system configurations, the development of multifunctional electrodes capable of facilitating multiple reactions at both the anode and the cathode concurrently is crucial.[9,61,68] Motivated by these requirements, we applied the GDE-Pd/NiO catalyst to the EtOR. The performance was assessed using CV in a three-electrode setup with an electrolyte of 1 M KOH and 1 M ethanol at a sweep rate of 50 mV s^{-1}, as shown in Fig. 5d–f and S8a† (forward scan for clear observation).

Ethanol oxidation initiates with the adsorption of hydroxyl species ($M{-}OH_{ads}$) and ethanol-derived species ($M{-}CH_3CH_2O_{ads}$) on the catalyst surface, proceeding through two primary pathways: the poisoning-intermediate (CO) pathway and the reactive-intermediate pathway.

CO pathway:

$$CH_3CH_2OH \rightarrow CH_3CHO_{ads} \rightarrow CO_{ads}, CH_{x,ads} \rightarrow CO_2 \text{ or } CO_3^{2-}$$

Reactive-intermediate pathway:

$$CH_3CH_2OH \rightarrow CH_3CHO_{ads} \rightarrow CH_3CHO/CH_3COOH \text{ or } CH_3COO^-$$

In the process of the EtOR, the formation of CO species severely limits the utilization efficiency and durability of the catalysts. CO can strongly adsorb onto the catalyst surface, blocking active sites and hindering catalytic activity. Therefore, according to the bifunctional mechanism valid for palladium-nickel catalysts, nickel promotes the formation of OH_{ads} species at low potentials for high CO tolerance by quickly scavenging the adsorbed CO species and leading to enhanced catalytic efficiency for the EtOR.[65,69–71] The reactive-intermediate pathway involves the formation of acetaldehyde (CH_3CHO) and acetic acid (CH_3COOH) as intermediates, which are further oxidized to CO_2.[72] This pathway is favored by the presence of sufficient OH_{ads} species, which assist in the removal of hydrogen atoms from the ethanol molecule and its intermediates, facilitating oxidation without forming strongly adsorbed CO intermediates. NiO can adsorb water molecules and facilitate their dissociation to generate OH_{ads} species through the formation of $Ni(OH)_2$ and NiOOH, which are essential for the oxidation of ethanol and the removal of poisoning intermediates.[71] In contrast, the poisoning-intermediate pathway involves the formation of CO as an intermediate, which can strongly adsorb onto the catalyst surface and block active sites, reducing the overall catalytic efficiency. To sum up, according to the bifunctional mechanism, the surface hydroxyl (OH_{ads}) species or the oxygen-containing species such as NiO can facilitate the incomplete ethanol oxidation to acetic acid and CO_2. Additionally, the anti-poisoning properties of NiO (by promoting the dissociative adsorption of water molecules and subsequent oxidative removal of CO intermediates) reduce the accumulation of

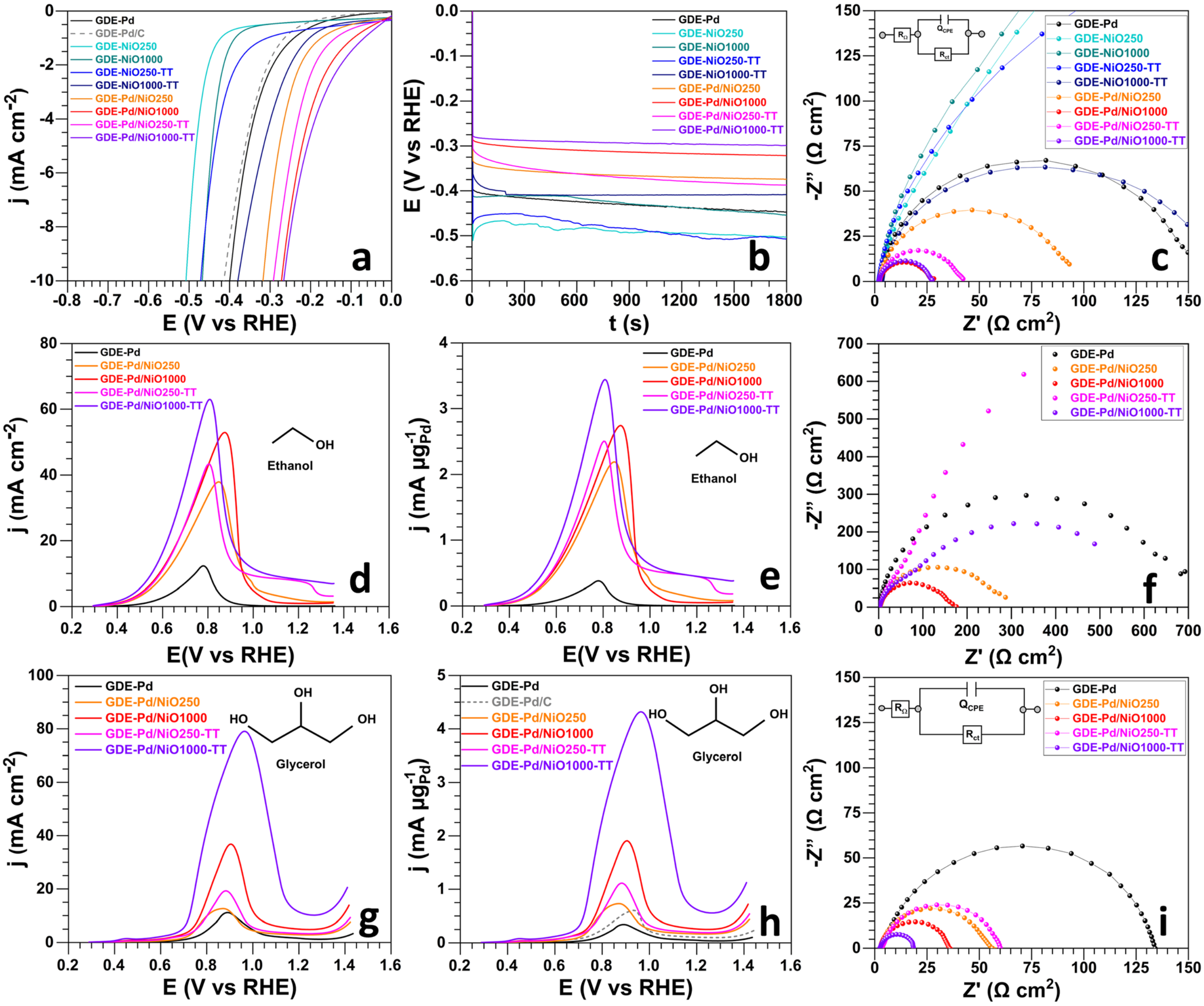

Fig. 5 Electrochemical performance of the as-synthesized GDE-Pd/NiOX and commercial Pd/C electrodes. (a) LSV curves for the HER (5 mV s^{-1}, 1 M KOH, and 25 °C). (b) Chronopotentiometry at a current density of $|j| = 10$ mA cm^{-2}. (c) Nyquist impedance plots at −0.18 V *vs.* RHE for the HER, (d and e) forward scans of the CV for the EtOR, with current density normalized to the geometric area (d) and metal loading (e), recorded at a scan rate of 50 mV s^{-1} in 1 M ethanol and 1 M KOH at 25 °C. (f) Nyquist impedance plots at 0.42 V *vs.* RHE for the EtOR. (g and h) Forward scans of the CV for the GOR, with current density normalized to the geometric area (g) and metal loading (h), recorded at a scan rate of 50 mV s^{-1} in 1 M glycerol and 1 M KOH at 25 °C. (i) Nyquist impedance plots at 0.67 V *vs.* RHE for the GOR. Potentials are ohmic-drop uncorrected.

poisoning intermediates on the catalyst surface and maintain high catalytic activity over prolonged periods.[31,71]

As shown in Fig. 5d, the bimetallic electrodes demonstrated a higher current density and a lower onset potential of approximately 0.30 V *vs.* RHE compared to the GDE-Pd electrode, which exhibited an onset potential of around 0.42 V *vs.* RHE. The enhanced electrocatalytic performance of the bimetallic GDE-Pd/NiO electrodes is due to the synergistic interplay between Pd and NiO components. The formation of $Ni(OH)_2$ and NiOOH from NiO enhances the generation of OH_{ads}, improving CO tolerance, while Pd efficiently adsorbs and oxidizes ethanol. Fig. 5e displays the current density normalized by Pd content (Table S4† gathers the peak current density normalized by either the geometric surface area or the estimated electrochemically active surface area (ECSA) of Pd), revealing the intrinsic catalytic activity of the electrodes. After normalizing for metal loading, the bimetallic electrodes outperformed GDE-Pd, underscoring the catalytic efficiency and superior Pd utilization achieved through Pd/NiO synergy. Furthermore, as demonstrated by EIS (Fig. 5f), the bimetallic electrodes exhibit enhanced electron transfer during the oxidation process, reflected in lower charge transfer resistance, thereby boosting catalytic activity.[61,64] This integration enhances the electrocatalytic properties, facilitating more efficient ethanol oxidation and contributing to the overall effectiveness of the energy conversion process. Thermal treatment further augments these effects by ensuring a uniform nanoparticle distribution, enhanced structural integrity and most importantly, the formation of Ni/NiO. This results in a more efficient, stable, and effective electrocatalyst for ethanol oxidation in biofuel applications and sustainable energy conversion technologies. Additionally, the peak current density for the thermally treated GDE-Pd/NiOX-TT electrodes was notably higher and occurred at a reduced potential of 0.6 V *vs.* RHE, compared to the untreated GDE-Pd/NiOX electrodes, which peaked at 0.7 V *vs.* RHE. This enhancement in electrocatalytic performance can be attributed to the structural and compositional modifications induced by thermal treatment, which lead to several synergistic effects that improve the efficiency of the EtOR. This reduction in peak potential signifies a more efficient catalytic process. Such a shift indicates that thermal treatment did not result in a unique phase PdNi alloy, as XPS and TEM results suggest, but rather led to a heterogeneous structure composed of PdNi with segregated phases of Pd and Ni. This configuration not only improves the dispersion of nanoparticles but also enhances the interaction between the reactant molecules and the catalytic species. The optimized electronic structure facilitates better adsorption and activation of ethanol, significantly reducing energy input requirements and enhancing the overall efficiency of the electrochemical system.

3.2.3 Electrocatalytic GOR performance. It appears that alcohols with more adjacent hydroxyl groups tend to exhibit higher activities.[73] Furthermore, monohydric alcohols have a smaller number of hydroxyl groups compared with diols and tri-alcohols at the same concentration, leading to the lower activity of ethanol and methanol compared with ethylene glycol, 1,2-propanediol, and glycerol.[73] Motivated by the promising ethanol oxidation activity of the previously discussed electrocatalysts, we further explored their application for glycerol oxidation, which involves a similar anodic proton/electron transfer process. Glycerol, with its high reactivity attributed to adjacent hydroxyl groups, can be oxidized to various valuable industrial intermediates/products.[19] The electrocatalytic activities of the electrodes for the GOR were evaluated using CV in a three-electrode setup with an electrolyte of 1 M KOH and 1 M glycerol at a sweep rate of 50 mV s^{-1}, as presented in Fig. 5g–h and S8b.†

As a polyol, glycerol undergoes complex, multi-step oxidation pathways involving multiple C–H and C–C bond cleavages at high potentials[3,74–77] and thus requires a high density of accessible and active catalytic sites for efficient conversion. The role of the NiOOH/Ni(OH)$_2$ redox couple is crucial in such processes occurring above 1.3–1.4 V *vs.* RHE (Fig. S6b†), meaning that this is valid only for monometallic Ni electrodes. According to the literature, this couple facilitates the so-called chemical–electrochemical mechanism for polyol oxidation, including glycerol.[63,78] Under anodic polarization, Ni(OH)$_2$ is converted to NiOOH, which then acts as an active oxidizing species, assisting in the dehydrogenation and subsequent oxidation of adsorbed glycerol intermediates, which is known as mediated electrocatalysis. *In situ* FTIR spectroscopy, as reported by Oliveira *et al.*,[78] has further confirmed that the formation of NiOOH coincides with the onset of glycerol oxidation (Fig. S6b *vs.* S8†) and the emergence of oxidation products. Thus, the presence of NiOOH/Ni(OH)$_2$ species on the catalyst surface enhances the oxidation kinetics by promoting adsorption and activation of glycerol, facilitating the cleavage of C–H and C–C bonds, and preventing poisoning from organic intermediates.

As shown in Fig. 5g, the incorporation of NiO into the Pd-based electrode followed by thermal treatment leads to a marked enhancement in GOR activity, which is explained by the aforementioned bifunctional mechanism. Indeed, within a palladium–nickel based electrode material, nickel promotes the formation of OH$_{ads}$ species at low potentials (0.3–1 V *vs.* RHE) for direct electrooxidation instead of the mediated electrocatalysis that needs a potential of 1.2–1.4 V *vs.* RHE, where NiOOH/Ni(OH)$_2$ is formed (Fig. S6b *vs.* S8†). The onset potential for glycerol oxidation on GDE-Pd is approximately 0.42 V *vs.* RHE, with a peak current density of 11 mA cm^{-2}. The catalytic activity of this electrode is enhanced by the presence of NiO, which improves both the onset potential and peak current. Specifically, the onset potential for GDE-Pd/NiO1000 is reduced to approximately 0.32 V *vs.* RHE, while the peak current density increases significantly to 37 mA cm^{-2}. After thermal treatment, the onset potential decreases to 0.30 V *vs.* RHE, and the peak current density increases two times (79 mA cm^{-2}), indicating substantial improvement in electrocatalytic performance.

These improvements can be attributed to several factors. The electrochemically active surface area (ECSA) increases after NiO incorporation and thermal treatment, as shown in Table S4.† The ECSA quantifies the effective surface area available for electrochemical reactions by estimating the coulombic charge associated with the reduction of palladium oxide in CV curves.[62] A larger ECSA means more available active sites for the GOR, contributing to higher catalytic activity. NiO acts as an electronic promoter, enhancing charge transfer between the catalyst and glycerol molecules. The electronic properties of the catalyst enhanced by incorporation of NiO and thermal treatment result in a more uniform distribution of Pd and Ni nanoparticles. This uniformity ensures accessible active sites and efficient handling of reaction intermediates. The well-dispersed NiO layer surrounding the Pd nanoparticles stabilizes the catalyst by preventing agglomeration, maintaining a high surface area and catalytic activity. In contrast, untreated GDE-Pd/NiOX electrodes show higher onset potentials and lower catalytic activity due to agglomerated and unevenly distributed Pd and NiO particles. The amorphous NiO layer formed during thermal treatment stabilizes the nanoparticles and enhances performance. These enhancements are further confirmed by EIS measurements, as shown in Fig. 5i and Table S5.† The Nyquist plots reveal that the thermally treated bimetallic electrodes exhibit a lower charge transfer resistance, indicated by a smaller semicircle radius (Fig. 5i), compared to untreated electrodes. A lower radius of the semicircle corresponds to higher charge transfer efficiency, demonstrating improved electron transfer between the catalyst surface and glycerol molecules. These findings demonstrate that optimized bimetallic compositions and thermal treatment significantly improve the performance of electrocatalysts for glycerol oxidation, highlighting the importance of catalyst design and post-treatment processes in sustainable energy applications.

3.2.4 Stability tests and GOR electrooxidation pathways in an H-type cell.

To further evaluate the long-term durability of the GDE-Pd/NiO1000-TT electrocatalyst under extended electrochemical operation, a 68-hour galvanostatic operation was conducted at an applied current $|I_{\text{applied}}|$ of 100 mA (corresponding to a current density $|j_{\text{applied}}|$ of 50 mA cm^{-2}) under HER conditions. The experiment was carried out in an H-type electrochemical cell, in which the anode and cathode compartments (each containing 1 M KOH) were separated by a Sustainion® X37-50 Grade RT anion exchange membrane. The electrolytes were periodically refreshed and preserved for post-mortem ICP-OES analysis. As shown in Fig. 6a, a slight increase in potential is observed during the initial phase of electrolysis, which may be attributed to transient effects such as hydrogen bubble accumulation at the electrode surface and the intrinsic hydrogen absorption capability of Pd, slightly hindering catalytic activity.[79] Following this initial stabilization period, the potential exhibits a near-steady trend. Interestingly, upon electrolyte replacement, the electrode potential temporarily decreased to values comparable to the initial stage of electrolysis, indicating the absence of catalyst degradation and minimal electrolyte-related performance loss. This behavior is likely attributed to the removal of accumulated hydrogen bubbles and possible degradation products at the electrode surface, as well as the restoration of ionic conductivity and homogeneity within the electrolyte. This transient recovery further confirms that the observed long-term stability is not due to passive surface blocking or electrolyte degradation, but rather reflects the intrinsic durability of the electrocatalyst. Over the full duration of the 68-hour test, no significant or abrupt increase in potential is observed, supporting the excellent long-term electrochemical stability of the catalyst under continuous alkaline HER operation.

To further understand the structural evolution of the GDE-Pd/NiO1000-TT catalyst during extended HER operation, comparative analyses were performed before and after the 68-hour electrolysis. Prior to electrochemical testing, TEM and selected area electron diffraction (SAED) analyses (Fig. S9–10†) confirmed the formation of a well-defined core–shell architecture with crystalline Pd and NiO domains, resulting from the thermal treatment step. Elemental mapping showed a clear distribution of NiO surrounding Pd-rich regions. Following prolonged HER electrolysis, TEM images reveal that this core–shell structure remains largely preserved, with no signs of severe aggregation, collapse, or particle coarsening. The average particle size appears to remain nearly unchanged, suggesting

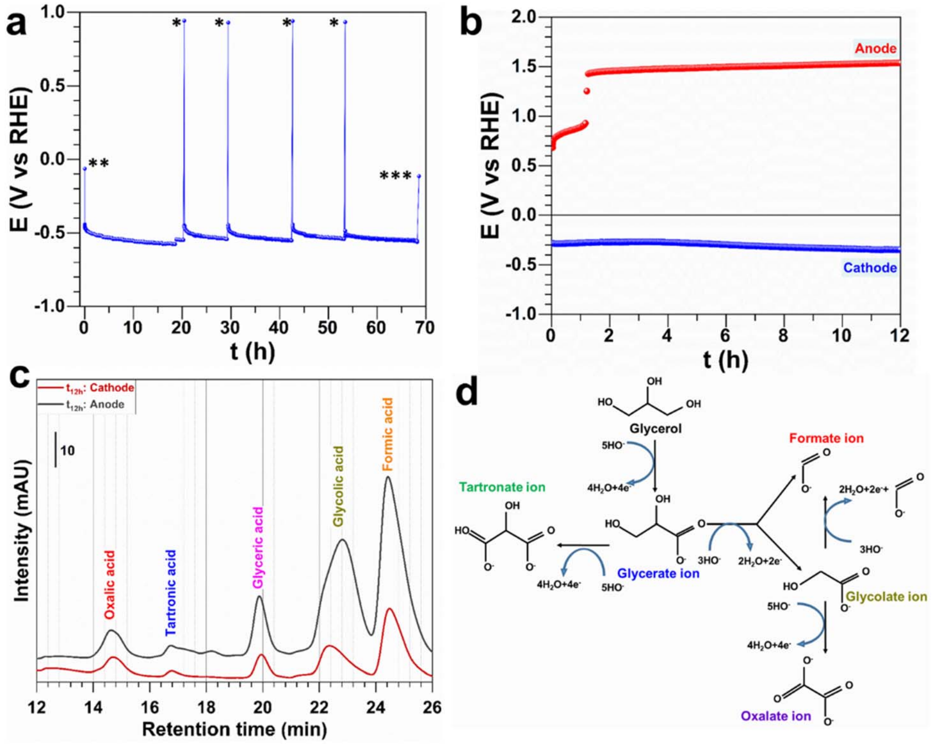

Fig. 6 Electrolysis in an H-type cell. (a) Chronopotentiometry recorded during 68 hours of electrolysis operation at an applied current $|I_{\text{applied}}|$ of 100 mA (corresponding to a current density $|j_{\text{applied}}|$ of 50 mA cm^{-2}, temperature: 25 °C, catholyte: 1 M KOH, anolyte: 1 M KOH (to avoid excessive consumption of glycerol during *ca.* 70 hours of operation), and hydroxide anion exchange membrane: Sustainion® X37-50 grade RT): * = electrolyte renewal (EC-Lab software with an SP-150 potentiostat from Biologic Science Instruments; the program was put on the "hold" position), **: start of program, and ***: end of the program. (b) Potentials of the anode and the cathode recorded during the galvanostatic operation at an applied current $|I_{\text{applied}}|$ of 20 mA (corresponding to a current density $|j_{\text{applied}}|$ of 10 mA cm^{-2}, temperature: 25 °C, catholyte: 1 M KOH, anolyte: 1 M KOH + 1 M glycerol, and hydroxide anion exchange membrane: Sustainion® X37-50 grade RT). (c) HPLC product distribution chromatograms (diluted by 10 times) after 12 h glycerol electrooxidation. (d) Proposed reaction pathways for the GOR in alkaline media at the synthesized electrocatalysts. Potentials and cell voltages are ohmic-drop uncorrected.

resistance to nanoparticle coarsening and structural degradation under alkaline HER conditions. SAED patterns still display reflections corresponding to Pd and NiO, alongside additional features attributed to metallic Ni, indicating partial reduction of NiO under such cathodic conditions. This transformation is consistent with expected behavior in strongly reducing electrochemical environments and further confirms the active nature of the catalyst. Post-mortem elemental mapping confirms continued co-localization of Pd and Ni, with minimal redistribution of elements. In addition, ICP-OES analysis of the post-electrolysis electrolyte is reported in Table S6†: (i) no significant amount of palladium was found in the electrolyte and (ii) 8.8% of the initial nickel amount was found within the electrolyte. These results collectively indicate that both the catalyst structure and elemental composition are well-maintained, and no major catalyst loss occurs either through dissolution or detachment during extended operation, confirming the excellent electrochemical and structural durability of the GDE-Pd/NiO1000-TT system under HER conditions.

Following a protocol similar to that reported by Knani *et al.*,[80] we designed a specific bulk electrolysis setup to monitor the anode and cathode potentials during galvanostatic operation, aiming to identify the limiting electrode by inserting a miniature reference electrode (RHE, MiniHydroFlex®, Bio-Logic) in each compartment (Fig. S11a†). The H-type cell incorporated a Sustainion® X37-50 Grade RT membrane to separate the anode compartment, containing 1 M KOH and 1 M glycerol, from the cathode compartment with 1 M KOH. For this experiment, the anode and cathode potentials were recorded at an applied current density of 10 mA cm^{-2}. This setup was chosen to allow for gradual glycerol oxidation, avoiding rapid depletion of glycerol in the solution (batch configuration) at larger current density. The GOR involves complex, multi-electron pathways and produces various intermediates that can adsorb onto the catalyst surface, affecting overall efficiency. Fig. 6b shows the evolution of anode and cathode potentials over 12 h of bulk electrolysis (Fig. S11b† reports the first 1.5 h). The anode potential gradually increased from 0.8 to 0.9 V *vs.* RHE during the first hour and stabilized around 1.45 V *vs.* RHE over the next 11 h. In contrast, the cathode potential remained stable near −0.30 V *vs.* RHE, indicating that the cathodic process was not the limiting factor in cell performance; instead, the anode reactions predominantly influenced cell potential and efficiency.

The initial increase in anode potential after the first hour likely results from the accumulation of reaction intermediates and partial catalyst deactivation. Glycerol oxidation generates various partially oxidized species, such as glycerate, glycolate and formate, which can adsorb onto the catalyst surface and block active sites, thereby raising overpotentials needed to sustain the current density. As the reaction proceeds, the catalyst surface undergoes restructuring or partial regeneration, likely due to the desorption of intermediates and the formation of more fully oxidized products. The stabilization of the anode potential around 1.5 V *vs.* RHE suggests a dynamic equilibrium between the formation and removal of these intermediates, enabling further oxidation of adsorbed species and the production of major oxidation products.

High-performance liquid chromatography (HPLC) was used to analyze the electrolyte solutions after 12 h of electrolysis (Fig. 6c) to elucidate the glycerol electrooxidation mechanism (Fig. 6d).[17] The chromatograms of Fig. 6c show the presence of various oxidation intermediates, in both anode and cathode compartments. The evaluated crossover, that is, $n_{(\mathrm{cathode})}/[n_{(\mathrm{anode})} + n_{(\mathrm{cathode})}]$ (n: is the number of moles), is 22–30% depending on the nature of the compound. The detection of these intermediates in both compartments suggests that some oxidation products permeated through the hydroxide AEM. Although the used membrane (Sustainion® X37-50 Grade RT (50 μm dry thickness), Fuel Cell Store (USA)) is designed to selectively transport hydroxide ions, it may not completely prevent the crossover of relatively small carboxylate ions from the anodic compartment to the cathodic one, especially under prolonged electrolysis conditions. This crossover can impact the overall efficiency of the electrolyzer by introducing unwanted side reactions in the cathode compartment and reducing the purity of hydrogen gas produced (unlikely in alkaline environments as all products are non-volatile). The presence of organic species at the cathode could also affect the HER kinetics by adsorbing onto the cathode surface.[81] Therefore, membrane optimization is crucial to minimize such permeation. Selecting membranes with improved selectivity and reduced porosity to organic molecules can enhance system performance by preventing crossover, ensuring product purity and maintaining efficient operation of both anodic and cathodic processes. This aspect is vital for the practical application of biomass-fed electrolyzers, where the integrity of the membrane directly affects the efficiency and sustainability of the system.

The identified reaction products for the GDE-Pd/NiO1000-TT electrode are shown in Fig. 6d and S12,† with quantitative metrics derived from calibration curves (Fig. S13†) and detailed in Fig. S14.† Two primary pathways are proposed for glycerol electrooxidation in alkaline media depending on the nature of the electrode material. The first pathway is direct oxidation, where the applied potential drives glycerol electrooxidation without altering the catalyst's valence state. This pathway involves progressive dehydrogenation of glycerol *via* adsorbed hydroxyl species, with C–H bond cleavage in terminal carbon groups, resulting in products like glycerate and tartronate at lower applied potentials (Fig. 6d). These products suggest that the catalyst favors pathways that retain the three-carbon backbone, important for producing valuable intermediates used in pharmaceuticals and fine chemicals. The second pathway is indirect oxidation, where the applied potential induces a valence change in the catalyst, allowing it to act as a redox mediator for glycerol oxidation. In Ni-based electrocatalysts, for example, the $NiOOH/Ni(OH)_2$ redox transition plays a central role, where Ni serves as an intermediate redox center undergoing valence changes to drive the reaction.[78] In Pd/NiO-based electrodes, the Ni component enhances electron transfer and oxidation activity, especially when the applied current increases the electrode potential above 1 V *vs.* RHE. At these elevated potentials, redox cycling between Ni(II) and Ni(III) actively facilitates glycerol oxidation; however, the main driving force is the bifunctional mechanism (detailed above). The incorporation of NiO also improves resistance to poisoning by organic intermediates that typically form during glycerol oxidation. This resistance is due to NiO's ability to modulate electron density within the Pd matrix (evidenced by XPS and DFT calculations), thereby sustaining catalytic activity despite the buildup of intermediates on the catalyst surface. The post-mortem analysis of the GDE-Pd/NiO1000-TT electrodes is essential for understanding the stability of the electrocatalyst changes after glycerol oxidation. Post-mortem analysis of the GDE-Pd/NiO1000-TT electrodes was conducted to assess electrocatalyst stability following glycerol oxidation. SEM and EDX mapping (Fig. S15–S16†) indicated no substantial morphological degradation or nanoparticle coalescence post-electrolysis, suggesting a robust physical structure. EDX-mapping images (Fig. S16†) provided detailed elemental distribution across the electrode surface. Notably, a reduction in NiO content was observed on the cathode surface, indicating some material loss during operation. However, the bimetallic composition remained stable across the electrode, with no significant compositional changes detected in the bimetallic structure.

3.2.5 Zero-gap AEM-based electrolyzer and H_2 collection. The GDE-Pd/NiO1000-TT electrode has demonstrated its significant potential in enhancing the efficiency of organic electrooxidation and the hydrogen evolution reaction. To validate its performance, practical tests were conducted using a zero-gap hydroxide anion exchange membrane (AEM)-based electrolyzer, in which the multifunctional GDE-Pd/NiO1000-TT electrode functioned as both the anode and the cathode in a two-electrode configuration. The ALD process streamlined the fabrication of these multifunctional electrodes without the need for catalytic ink fabrication for traditional approaches, simplifying the electrolyzer design and substantially boosting system efficiency. The zero-gap design minimized ohmic losses for 1 M ethanol (1.2 Ω cm^2) and for 1 M glycerol (0.9 Ω cm^2) by reducing the distance between the anode and the cathode. Additionally, the flowing electrolyte enhanced mass transport, optimizing the electrolyzer's performance.[38,82,83] The polarization curves for the zero-gap AEM-based ethanol and glycerol electrolyzers were obtained, comparing the performance of the GDE-Pd/NiO1000-TT electrode at different temperatures using both the potentiostatic method (0.1 V step) and the galvanostatic method (0.05 V s^{-1} scan rate), as illustrated in Fig. 7a–d and S17.† Comparison of polarization curves from control experiments, with and without organic molecules, revealed that the addition of biomass to the anolyte significantly reduced the voltage required to achieve comparable current density ($U < 0.8$ V), as shown in Fig. 7a. This voltage reduction is attributed to the lower thermodynamic and kinetic barriers for oxidizing organic molecules compared to water oxidation, making the process more energy-efficient.

In the ethanol-fed electrolyzer, the GDE-Pd/NiO1000-TT electrode achieved a current density of 10 mA cm^{-2} at cell voltages of 0.75 and 0.7 V at 26 and 50 °C, respectively (Fig. 7b). At a current density of 100 mA cm^{-2}, cell voltages were 1.1 V and 1.2 V at 26 and 50 °C, respectively. Elevated temperatures enhance electrolyzer performance by increasing molecular kinetic energy, thereby accelerating the rates of the EtOR and HER. This results in higher current densities at lower overpotentials. Moreover, increased temperatures decrease electrolyte viscosity, enhancing reactant diffusion (ethanol and hydroxide ions) to the electrode surfaces and product removal, which mitigates concentration polarization effects and improves performance at elevated temperatures. In the glycerol-fed electrolyzer, the GDE-Pd/NiO1000-TT electrode exhibited lower overpotentials with increasing temperature, achieving 100 mA cm^{-2} at 1.31 and 1.22 V at 50 and 70 °C, respectively, confirming improved kinetics (Fig. 7c). The post-mortem analysis of the GDE-Pd/NiO1000-TT electrodes was conducted to assess electrocatalyst stability following electrolysis of biomasses. SEM and EDX mapping (Fig. S18†) indicated no substantial morphological degradation or nanoparticle coalescence post-electrolysis, suggesting a robust physical structure. EDX mapping (Fig. S18†) provided detailed elemental distribution across the electrode surface. Notably, a reduction in NiO content was observed on the anode surface, indicating some material loss during operation. However, the bimetallic composition remained stable across the electrode, with no significant compositional changes detected in the alloy structure.

Further analysis revealed distinct electrocatalytic behaviors between the GDE-Pd and GDE-Pd/NiO1000-TT electrodes in both biomass-fed electrolyzers, as shown in Fig. 7d. The GDE-Pd electrode requires a higher driving voltage to achieve substantial activity, indicating lower catalytic efficiency. In contrast, integrating NiO and applying thermal treatment enhance the Pd-based catalyst's efficiency by modifying the electronic structure and introducing additional active sites, which facilitate the adsorption and activation of ethanol and glycerol molecules. The bifunctional interaction between Pd and NiO/Ni enables more effective C–H and O–H bond cleavage, reducing onset potentials and increasing current density due to enhanced electron transfer and oxidation kinetics. Additionally, NiO's anti-poisoning properties prevent intermediates from blocking active sites, sustaining continuous catalytic activity and accelerating reaction kinetics at elevated potentials. These combined effects stabilize the catalyst, extend its operational range, and improve overall performance. EIS results (Fig. S19 and Tables S7 and S8†) offer further insight into the electrocatalytic dynamics of the system, particularly in terms of charge transfer resistance, ohmic losses, and related phenomena. The Nyquist plots obtained at different temperatures, modeled with an equivalent circuit ($R_\Omega + Q_{\text{CPE-a}}//R_{\text{ct-a}} + Q_{\text{CPE-c}}//R_{\text{ct-c}}$, where "a" refers to the anode and "c" refers to the cathode), reveal distinct characteristics of the ethanol-fed and glycerol-fed electrolyzers. In both electrolyzers as shown in Fig. S19,† the overall ohmic resistance (R_Ω) decreased with increasing temperature, indicating improved ionic conductivity of the electrolyte and reduced resistance of the membrane at higher temperatures. Notably, the $R_{\text{ct-a}}$ dropped significantly as temperature rose, suggesting enhanced kinetics of organic oxidation due to increased catalytic activity and accelerated reaction rates at

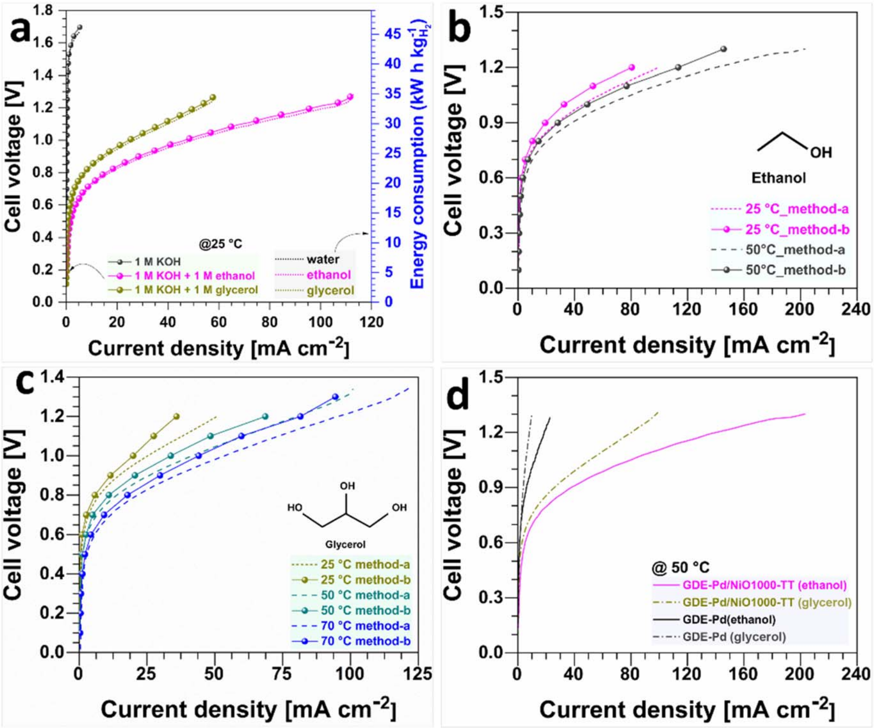

Fig. 7 Zero-gap electrolyzer performance. (a) Polarization curves of GDE-Pd/NiO1000-TT ‖ GDE-Pd/NiO1000-TT highlighting the effect of the presence of biomass (LSV method, 0.05 V s^{-1} scan rate). (b and c) Polarization curves of GDE-Pd/NiO1000-TT ‖ GDE-Pd/NiO1000-TT highlighting the effect of temperature with the galvanostatic method (step of 0.05 V, method-2) and potentiostatic method (0.05 V s^{-1} scan rate, method-1). (d) Polarization curves of GDE-Pd/NiO1000-TT ‖ GDE-Pd/NiO1000-TT and GDE-Pd ‖ GDE-Pd potentiostatic methods, 0.05 V s^{-1} scan rate. Catholyte: 1 M KOH (45 mL min^{-1}). Anolyte: 1 M KOH + 1 M glycerol or ethanol (23 mL min^{-1}). Hydroxide anion exchange membrane: Sustainion® X37-50 grade RT (5 cm^2). Potentials and cell voltages are ohmic-drop uncorrected.

elevated temperatures. These EIS results support the polarization data, confirming that higher temperatures boost electrolyzer performance by accelerating reaction kinetics and reducing charge transfer resistance at both electrodes. The glycerol-fed electrolyzer showed a more pronounced reduction in $R_{\text{ct-a}}$ than the ethanol-fed one, likely due to the complex oxidation pathways of glycerol, which gain more from higher temperatures to overcome kinetic barriers. To quantify the temperature dependence of activation energy and reaction kinetics, Arrhenius plots were constructed using charge transfer resistance values from EIS data (Fig. S20†). The linearity of the Arrhenius plot for the GDE-Pd/NiO1000-TT electrode across various temperatures indicates typical Arrhenius behavior. The slope of the plot, when multiplied by the gas constant ($R = 8.314$ J mol^{-1} K^{-1}), yields an activation energy of 27.9 kJ mol^{-1} for the GOR at the anode. While EtOR performance was evaluated at 26 °C and 50 °C, a full Arrhenius analysis was not performed. The restricted temperature range and ethanol's volatility at elevated temperatures (≥70 °C) limited the collection of reproducible EIS data.

It is worth noting that the results differ in the three-electrode configuration and the two-electrode setup. Specifically, higher current densities were observed for the GOR in the three-electrode setup, while the EtOR exhibited higher current densities in the two-electrode setup (a comparison of electrocatalytic performances in a half-cell and electrolyzer with the literature is reported in Tables S9–S12,† which highlight the promising aspect of the ALD method for developing electrocatalysts). In a two-electrode system, factors such as electrode spacing, flow dynamics, and balance of reactions at both electrodes can create an environment that influences the overall catalytic performance. Conversely, the three-electrode setup allows for more precise control and measurement of individual electrode behavior but may not fully capture the dynamics of a practical cell environment. Therefore, it is essential to analyze electrodes in both configurations to fully understand their catalytic behavior and optimize performance across different applications. To validate our system's efficiency in maintaining a cell voltage below 1 V while generating H_2, hydrogen flow rates were measured using the water displacement method with a fixed current of 250 mA (50 mA cm^{-2} for comparable analysis across all electrodes). Performance comparisons were made using the GDE-Pd/NiO1000-TT electrode in ethanol- and glycerol-fed electrolyzers, with the theoretical hydrogen production curve as a reference (Fig. S21†). The results indicate that the GDE-Pd/NiO1000-TT electrode achieved about 87% of the theoretical maximum, closely aligning with theoretical values. These findings highlight the necessity of continuous optimization in both electrolyzer design and operation. Despite these technical challenges, the achieved efficiency underscores the effectiveness of both electrocatalysts and electrolyzer design in hydrogen production, offering insights into areas for future enhancements to further improve efficiency and practical viability.

4. Conclusion

This study highlights the significant advancements achieved through the development and optimization of GDE based palladium and nickel electrodes for electrocatalytic applications. Specifically, by incorporating Pd between NiO species and carbon microfibers with the ALD method and applying thermal treatment as a free-standing approach to design electrocatalytically active multifunctional GDE-Pd/NiO1000-TT electrodes (ultra-low metal loading estimation of about 20 μg_{Pd} cm^{-2} and 47 μg_{Pd+Ni} cm^{-2}), we observed performance improvement in the HER as well as EtOR and GOR. The synergy between Pd and NiO not only enhances the electronic structure, supported by DFT calculations, but also provides additional active sites, leading to superior catalytic performance. The fabrication of these multifunctional electrodes *via* ALD simplifies their production and enhances their practical applicability in zero-gap hydroxide AEM-based electrolyzers. This configuration minimizes ohmic losses and improves mass transport, thereby optimizing the electrolyzer's overall performance. Our results demonstrated that GDE-Pd/NiO1000-TT electrodes exhibit lower onset potentials and higher current densities compared to their monometallic counterparts, underscoring the benefits of the bimetallic structure and thermal treatment. In ethanol-fed electrolyzers, the GDE-Pd/NiO1000-TT structure facilitated the initiation of ethanol oxidation at a lower energy threshold, while in glycerol-fed electrolyzers, it provided enhanced reaction kinetics and anti-poisoning properties. These improvements were corroborated by the electrochemical impedance spectroscopy (EIS) analysis, which showed reduced charge-transfer resistances for the bimetallic samples, indicating more efficient electron transfer processes. The zero-gap electrolyzer tests confirmed the enhanced performance of GDE-Pd/NiO1000-TT electrodes in practical applications. The hydrogen production rates achieved were closely aligned with theoretical values, further validating the efficiency of these electrocatalysts. From an economic perspective, the ultra-low Pd loading combined with excellent structural stability during a 68-hour test at industrially relevant current density (100 mA) reduces material and replacement costs. Post-test analyses (TEM, SAED, EDS, and ICP-OES) confirmed minimal changes and negligible metal leaching, supporting long-term durability. While ALD faces scalability challenges (throughput and cost), our approach of precise, low-loading deposition and thermal treatment offers a promising route to practical, cost-effective electrode fabrication. Despite some technical challenges, the study highlights the potential of these optimized bimetallic compositions in advancing sustainable energy conversion technologies. Overall, the integration of more abundant nickel species and the application of thermal treatment have proven to be effective strategies for developing high-performance electrocatalysts. These findings provide valuable insights into the design and optimization of multifunctional electrodes, paving the way for more efficient and economically viable solutions in renewable energy applications. Future research should focus on further optimizing the electrode design and exploring their long-term stability and scalability in various electrochemical systems.

Data availability

The data that support the findings of this study are included in the published article and its ESI.†

Conflicts of interest

The authors declare that they have no known competing financial interests or personal relationships that could have appeared to influence the work reported in this paper.

Acknowledgements

The authors are grateful for financial support from LabEx CheMISyst (ANR-10LABX-05-01) and the French National Research Agency (ANR) as part of grant ANR-17-CE09-0049-03 (MENINA project). The authors thank Didier Cot, Bertrand Rebiere and Valerie Bonniol (IEM Montpellier) for assistance with SEM-EDX and HPLC analysis. The authors also thank Aurelien Renard (University of Lorraine, Nancy, France) for support and assistance during XPS analysis. The authors thank Maxime Dufond (Aix-Marseille Univ, CNRS) for assistance with the ellipsometry analysis. HG acknowledge the access to the HPC resources of CCRT/CINES/IDRIS, granted under the allocation A0170807369.

References

1 X. Ma, C. Guo, J. Xiang, Y. Qi, J. Yu, K. Li, Z. Tao, J. Wu and Y. Lv, *Int. J. Hydrogen Energy*, 2024, **60**, 845–866.
2 D. Parra, L. Valverde, F. J. Pino and M. K. Patel, *Renew. Sustain. Energy Rev.*, 2019, **101**, 279–294.
3 N. Tuleushova, Y. Holade, D. Cornu and S. Tingry, *Electrochem. Sci. Adv.*, 2023, **3**, e2100174.
4 C. Qiu, Z. Xu, F.-Y. Chen and H. Wang, *ACS Catal.*, 2024, **14**, 921–954.
5 W. Xi, P. Yang, M. Jiang, X. Wang, H. Zhou, J. Duan, M. Ratova and D. Wu, *Appl. Catal. B Environ.*, 2024, **341**, 123291.
6 Y. Holade, N. Tuleushova, S. Tingry, K. Servat, T. W. Napporn, H. Guesmi, D. Cornu and K. B. Kokoh, *Catal. Sci. Technol.*, 2020, **10**, 3071–3112.
7 Q. Qian, Y. Zhu, N. Ahmad, Y. Feng, H. Zhang, M. Cheng, H. Liu, C. Xiao, G. Zhang and Y. Xie, *Adv. Mater.*, 2024, **36**, 2306108.
8 Y. Li, Z. Dang and P. Gao, *Nano Sel.*, 2021, **2**, 847–864.
9 Y. X. Chen, A. Lavacchi, H. A. Miller, M. Bevilacqua, J. Filippi, M. Innocenti, A. Marchionni, W. Oberhauser, L. Wang and F. Vizza, *Nat. Commun.*, 2014, **5**, 4036.
10 S. S. Siwal, S. Thakur, Q. B. Zhang and V. K. Thakur, *Mater. Today Chem.*, 2019, **14**, 100182.

11 C. Chen, Z. Zhou, J. Liu, B. Zhu, H. Hu, Y. Yang, G. Chen, M. Gao and J. Zhang, *Appl. Catal. B Environ.*, 2022, **307**, 121209.

12 X. Liu, Y. Wang, Z. Dai, D. Gao and X. Zhao, *J. Energy Chem.*, 2024, **92**, 705–729.

13 J.-T. Ren, L. Chen, H.-Y. Wang, W.-W. Tian and Z.-Y. Yuan, *Energy Environ. Sci.*, 2024, **17**, 49–113.

14 M. Ayoub and A. Z. Abdullah, *Renew. Sustain. Energy Rev.*, 2012, **16**, 2671–2686.

15 Y. Li, X. Wei, L. Chen, J. Shi and M. He, *Nat. Commun.*, 2019, **10**, 5335.

16 Y. Yan, P. Hao, Y. Fu, W. Chen, Q. Shi, H. Zhou, X. Kong, Z. Li, M. Shao and X. Duan, *AIChE J.*, 2024, e18370.

17 A. Cassani, N. Tuleushova, Q. Wang, H. Guesmi, V. Bonniol, J. Cambedouzou, S. Tingry, M. Bechelany, D. Cornu and Y. Holade, *ACS Appl. Energy Mater.*, 2021, **4**, 9944–9960.

18 H. Yu, M. Hu, C. Chen, C. Hu, Q. Li, F. Hu, S. Peng and J. Ma, *Angew. Chem.*, 2023, **135**, e202314569.

19 T. Li and D. A. Harrington, *ChemSusChem*, 2021, **14**, 1472–1495.

20 Z. He, Q. Duan, C. Wang and L. Liao, *J. Colloid Interface Sci.*, 2023, **646**, 529–537.

21 G. Zhang, C. Hui, Z. Yang, Q. Wang, S. Cheng, D. Zhang, P. Cui and J. Shui, *Appl. Catal. B Environ.*, 2024, **342**, 123377.

22 Q. Li, X. Zhou, M. Lu, S. Pan, S. Ajmal, D. Xiang, Z. Sun, M. Zhu and P. Li, *J. Colloid Interface Sci.*, 2024, **653**, 1264–1271.

23 S. Yang, Z. Si, G. Li, P. Zhan, C. Liu, L. Lu, B. Han, H. Xie and P. Qin, *Small*, 2023, **19**, 2207651.

24 C. Lim, A. R. Fairhurst, B. J. Ransom, D. Haering and V. R. Stamenkovic, *ACS Catal.*, 2023, **13**, 14874–14893.

25 A. S. Bandarenka and M. T. M. Koper, *J. Catal.*, 2013, **308**, 11–24.

26 P. Strasser, S. Koh, T. Anniyev, J. Greeley, K. More, C. Yu, Z. Liu, S. Kaya, D. Nordlund, H. Ogasawara, M. F. Toney and A. Nilsson, *Nat. Chem.*, 2010, **2**, 454–460.

27 Y. Holade, C. Morais, S. Arrii-Clacens, K. Servat, T. W. Napporn and K. B. Kokoh, *Electrocatalysis*, 2013, **4**, 167–178.

28 E. Leal Da Silva, A. Cuña, C. Reyes Plascencia, C. Radtke, N. Tancredi and C. De Fraga Malfatti, *Clean Technol. Environ. Policy*, 2020, **22**, 259–268.

29 C. Xu, Y. Hu, J. Rong, S. P. Jiang and Y. Liu, *Electrochem. Commun.*, 2007, **9**, 2009–2012.

30 T. Maiyalagan and K. Scott, *J. Power Sources*, 2010, **195**, 5246–5251.

31 A. K. Ipadeola, N. Z. Lisa Mathebula, M. V. Pagliaro, H. A. Miller, F. Vizza, V. Davies, Q. Jia, F. Marken and K. I. Ozoemena, *ACS Appl. Energy Mater.*, 2020, **3**, 8786–8802.

32 A. Zalineeva, A. Serov, M. Padilla, U. Martinez, K. Artyushkova, S. Baranton, C. Coutanceau and P. Atanassov, *Electrochem. Commun.*, 2015, **57**, 48–51.

33 K. Cao, J. Cai, B. Shan and R. Chen, *Sci. Bull.*, 2020, **65**, 678–688.

34 C. Lausecker, D. Muñoz-Rojas and M. Weber, *Crit. Rev. Solid State Mater. Sci.*, 2023, 1–23.

35 A. J. M. Mackus, M. J. Weber, N. F. W. Thissen, D. Garcia-Alonso, R. H. J. Vervuurt, S. Assali, A. A. Bol, M. A. Verheijen and W. M. M. Kessels, *Nanotechnology*, 2016, **27**, 034001.

36 L. Assaud, E. Monyoncho, K. Pitzschel, A. Allagui, M. Petit, M. Hanbücken, E. A. Baranova and L. Santinacci, *Beilstein J. Nanotechnol.*, 2014, **5**, 162–172.

37 L. Assaud, N. Brazeau, M. K. S. Barr, M. Hanbücken, S. Ntais, E. A. Baranova and L. Santinacci, *ACS Appl. Mater. Interfaces*, 2015, **7**, 24533–24542.

38 M. Weber, N. Tuleushova, J. Zgheib, C. Lamboux, I. Iatsunskyi, E. Coy, V. Flaud, S. Tingry, D. Cornu, P. Miele, M. Bechelany and Y. Holade, *Appl. Catal. B Environ.*, 2019, **257**, 117917.

39 L. Assaud, N. Brazeau, M. K. S. Barr, M. Hanbücken, S. Ntais, E. A. Baranova and L. Santinacci, *ACS Appl. Mater. Interfaces*, 2015, **7**, 24533–24542.

40 A. Barhoum, H. H. El-Maghrabi, I. Iatsunskyi, E. Coy, A. Renard, C. Salameh, M. Weber, S. Sayegh, A. A. Nada, S. Roualdes and M. Bechelany, *J. Colloid Interface Sci.*, 2020, **569**, 286–297.

41 M. K. S. Barr, L. Assaud, Y. Wu, C. Laffon, P. Parent, J. Bachmann and L. Santinacci, *Electrochim. Acta*, 2015, **179**, 504–511.

42 T. W. Napporn, Y. Holade, B. Kokoh, S. Mitsushima, K. Mayer, B. Eichberger and V. Hacker, in *Fuel Cells and Hydrogen*, Elsevier, 2018, pp. 175–214.

43 A. Merenda, M. Weber, M. Bechelany, L. Hyde, L. Kong and L. F. Dumée, *Appl. Surf. Sci.*, 2019, **483**, 219–230.

44 M. Weber, P. Collot, H. El Gaddari, S. Tingry, M. Bechelany and Y. Holade, *ChemElectroChem*, 2018, **5**, 743–747.

45 H. L. Lu, G. Scarel, C. Wiemer, M. Perego, S. Spiga, M. Fanciulli and G. Pavia, *J. Electrochem. Soc.*, 2008, **155**, H807.

46 G. Kresse and J. Furthmüller, *Phys. Rev. B:Condens. Matter Mater. Phys.*, 1996, **54**, 11169–11186.

47 J. P. Perdew, K. Burke and M. Ernzerhof, *Phys. Rev. Lett.*, 1996, **77**, 3865–3868.

48 P. E. Blöchl, *Phys. Rev. B:Condens. Matter Mater. Phys.*, 1994, **50**, 17953–17979.

49 G. Kresse and D. Joubert, *Phys. Rev. B:Condens. Matter Mater. Phys.*, 1999, **59**, 1758–1775.

50 A. Hermawan, A. T. Hanindriyo, E. R. Ramadhan, Y. Asakura, T. Hasegawa, K. Hongo, M. Inada, R. Maezono and S. Yin, *Inorg. Chem. Front.*, 2020, **7**, 3431–3442.

51 S. Grimme, J. Antony, S. Ehrlich and H. Krieg, *J. Chem. Phys.*, 2010, **132**, 154104.

52 Y. Gao, L. Yan, C. Zhao, M. Chen, S. Yang, G. Shao and J. Mao, *J. Electrochem. Soc.*, 2024, **171**, 020558.

53 C. Badie, J.-H. Lee, A. Mirzaei, H. W. Kim, S. Sayegh, M. Bechelany, L. Santinacci and S. S. Kim, *J. Mater. Chem. A*, 2023, **11**, 12202–12213.

54 H. Liu, K. Tao, C. Xiong and S. Zhou, *Catal. Sci. Technol.*, 2015, **5**, 405–414.

55 M. Weber, C. Lamboux, B. Navarra, P. Miele, S. Zanna, M. E. Dufond, L. Santinacci and M. Bechelany, *Nanomaterials*, 2018, **8**, 849.

56 A. Karimaghaloo, J. Koo, H.-S. Kang, S. A. Song, J. H. Shim and M. H. Lee, *Int. J. Precis. Eng. Manuf.-Green Technol.*, 2019, **6**, 611–628.

57 J. Richardson, *Appl. Catal. Gen.*, 2003, **246**, 137–150.

58 Q. Jeangros, T. W. Hansen, J. B. Wagner, C. D. Damsgaard, R. E. Dunin-Borkowski, C. Hébert, J. Van Herle and A. Hessler-Wyser, *J. Mater. Sci.*, 2013, **48**, 2893–2907.

59 Q.-N. Ha, C.-H. Yeh, N. S. Gultom and D.-H. Kuo, *J. Mater. Chem. A*, 2024, **12**, 460–474.

60 M. M. Heath, M. Potgieter, F. Seland, S. Sunde and R. J. Kriek, *ChemElectroChem*, 2024, **11**, e202300485.

61 Y. Feng, D. Bin, B. Yan, Y. Du, T. Majima and W. Zhou, *J. Colloid Interface Sci.*, 2017, **493**, 190–197.

62 Y. Holade, T. W. Napporn, C. Morais, K. Servat and K. B. Kokoh, *ChemElectroChem*, 2015, **2**, 592–599.

63 V. L. Oliveira, C. Morais, K. Servat, T. W. Napporn, P. Olivi, K. B. Kokoh and G. Tremiliosi-Filho, *Electrocatalysis*, 2015, **6**, 447–454.

64 L. L. Carvalho, F. Colmati and A. A. Tanaka, *Int. J. Hydrogen Energy*, 2017, **42**, 16118–16126.

65 L. Chen, L. Lu, H. Zhu, Y. Chen, Y. Huang, Y. Li and L. Wang, *Nat. Commun.*, 2017, **8**, 14136.

66 K. Bhunia, K. Serbara Bejigo and S.-J. Kim, *Chem. Eng. J.*, 2024, **484**, 149306.

67 J. Ren, J. Zhang, C. Yang, Y. Yang, Y. Zhang, F. Yang, R. Ma, L. Yang, H. He and H. Huang, *Mater. Today Energy*, 2020, **16**, 100409.

68 L. Fan, Y. Ji, G. Wang, Z. Zhang, L. Yi, K. Chen, X. Liu and Z. Wen, *J. Energy Chem.*, 2022, **72**, 424–431.

69 T. Wu, X. Wang, A. Emrehan Emre, J. Fan, Y. Min, Q. Xu and S. Sun, *J. Energy Chem.*, 2021, **55**, 48–54.

70 J. W. Hong, Y. Kim, D. H. Wi, S. Lee, S. Lee, Y. W. Lee, S. Choi and S. W. Han, *Angew. Chem., Int. Ed.*, 2016, **55**, 2753–2758.

71 W. Huang, X. Ma, H. Wang, R. Feng, J. Zhou, P. N. Duchesne, P. Zhang, F. Chen, N. Han, F. Zhao, J. Zhou, W. Cai and Y. Li, *Adv. Mater.*, 2017, **29**, 1703057.

72 B. Cermenek, J. Ranninger, B. Feketeföldi, I. Letofsky-Papst, N. Kienzl, B. Bitschnau and V. Hacker, *Nano Res.*, 2019, **12**, 683–693.

73 N. Xi, Y. Zang, X. Sun, J. Yu, M. Johnsson, Y. Dai, Y. Sang, H. Liu and X. Yu, *Adv. Energy Mater.*, 2023, **13**, 2301572.

74 A. Zalineeva, A. Serov, M. Padilla, U. Martinez, K. Artyushkova, S. Baranton, C. Coutanceau and P. B. Atanassov, *J. Am. Chem. Soc.*, 2014, **136**, 3937–3945.

75 R. P. Durbin, *Am. J. Physiol.*, 1975, **229**, 1726.

76 H. Koshiba, *Jpn. J. Pharmacol.*, 1975, **71**, 415–426.

77 H. Luo, V. Y. Yukuhiro, P. S. Fernández, J. Feng, P. Thompson, R. R. Rao, R. Cai, S. Favero, S. J. Haigh, J. R. Durrant, I. E. L. Stephens and M.-M. Titirici, *ACS Catal.*, 2022, **12**, 14492–14506.

78 V. L. Oliveira, C. Morais, K. Servat, T. W. Napporn, G. Tremiliosi-Filho and K. B. Kokoh, *Electrochim. Acta*, 2014, **117**, 255–262.

79 Y. Chen, Y. Hou, G. Govor, O. Demidenko and Y. Li, *ChemElectroChem*, 2024, **11**, e202400071.

80 S. Knani, M. Tauk, P. Hajjar, M. Lacour, M. Shahrokhi, C. Canaff, C. Morais, S. Morisset, P. Huguet, D. Cot, B. Rebiere, E. Oliviero, V. Bonniol, J. Cambedouzou, M. Bechelany, S. Tingry, K. B. Kokoh, T. W. Napporn, H. Guesmi, D. Cornu and Y. Holade, *Small Struct.*, 2024, 2400276.

81 C. Dai, Q. Wu, T. Wu, Y. Zhang, L. Sun, X. Wang, A. C. Fisher and Z. J. Xu, *Energy Environ. Sci.*, 2024, **17**, 6350–6359.

82 R. Phillips, A. Edwards, B. Rome, D. R. Jones and C. W. Dunnill, *Int. J. Hydrogen Energy*, 2017, **42**, 23986–23994.

83 W. Wu, Z. Tang, K. Wang, Z. Liu, L. Li and S. Chen, *Electrochim. Acta*, 2018, **260**, 168–176.